1 Overview

1.1 Direct Detection of Dark Matter

During the past two decades, a standard cosmological picture of the universe (the Lambda Cold Dark Matter or LCDM model) has emerged, which includes a detailed breakdown of the main constituents of the energy density of the universe. This theoretical framework is now on a firm empirical footing, given the remarkable agreement of a diverse set of astrophysical data [1, 2]. Recent results by Planck largely confirm the earlier Wilkinson Microwave Anisotropy Probe (WMAP) conclusions and confirm that the universe is spatially flat, with an acceleration in the rate of expansion and an energy budget comprising approximately 5 % baryonic matter, 26 % cold dark matter (CDM), and roughly 69 % dark energy [3–5]. With the generation-2 (G2) dark matter experiments, we are now in a position to identify this dark matter through sensitive terrestrial *direct detection* experiments. Failing to detect a signal in G2, or in subsequent generation (G3), experiments would rule out most of the natural parameter space that describes weakly interacting massive particles (WIMPs), forcing us to reassess the WIMP paradigm and look for new detection techniques. In the following sections, we introduce the cosmological and particle physics evidence pointing to the hypothesis that the dark matter is composed of WIMPs, detectable through nuclear recoil (NR) interactions in low-background experiments. We then give the motivation for a massive liquid xenon (LXe) detector as the logical next step in the direct detection of dark matter.

1.1.1 Cosmology and Complementarity

While the Large Hadron Collider (LHC) experiments continue to verify the Standard Model of particle physics to ever-greater precision, the nature of the particles and fields that constitute dark energy and dark matter remain elusive. The gravitational effects of dark matter are evident throughout the cosmos, dominating gravitational interactions of objects as small as dwarf satellites of the Milky Way, up to galaxy clusters and superclusters. Application of Kepler's laws leads to the inescapable conclusion that our own galaxy, and all others, are held together by the gravitational pull of a dark halo that outweighs the combined mass of stars and gas by an order of magnitude, and appears to form an extended halo beyond the distribution of luminous matter.

At the same time, very weakly interacting CDM, particles or compact objects that were moving non-relativistically at the time of decoupling, appear to be an essential ingredient in the evolution of structure in the universe. N-body simulations of CDM can explain much of the structure, ranging from objects made of tens of thousands of stars to galaxy clusters. In the past few years, more realistic simulations, including both baryonic matter (gas and stars) and dark matter, are beginning to reveal how galaxy-like objects can arise from the primordial perturbations in the early universe [6, 7].

While we know much about the impact of dark matter on a variety of astrophysical phenomena, we know very little about its nature. An attractive conjecture is that dark matter particles were in equilibrium with ordinary matter in the hot early universe. We note, however, that there are viable dark matter candidates, including axions, where the conjecture of thermal equilibrium is not made [8]. Thermal equilibrium describes the balance between annihilation of dark matter into ordinary particle-antiparticle pairs, and vice versa. As the universe expanded and cooled, the reaction rates (the product of number density, cross section, and relative velocity) eventually fell below the level required for thermal equilibrium, leaving behind a relic

abundance of dark matter. The lower the annihilation cross section of dark matter into ordinary matter, the higher the relic abundance of dark matter. An annihilation cross-section characteristic of the weak interaction results in a dark matter energy consistent with that observed by cosmological measurements [9].

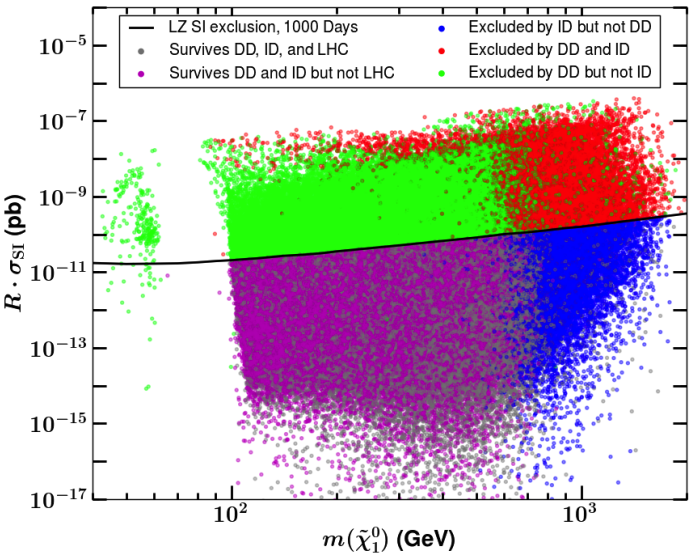

Figure 1.1.1: Scan of pMSSM parameter space and complementarity. Each point represents a SUSY model and is plotted as WIMP-nucleon scattering cross section scaled by abundance versus mass of the WIMP. The colors show models that can be tested by the three techniques of detection: direct detection (DD), LHC, and indirect detection (ID), and their combinations. The black curve shows the expected LZ sensitivity based on an early (2013) LZ estimate, weakened by a factor of four [10].

Models of supersymmetry (SUSY) predict the neutralino, a new particle that has properties appropriate to be a WIMP. SUSY posits a fermion-like partner for every Standard Model boson, and a boson-like partner for every Standard Model fermion. A principal feature of SUSY is its natural means for achieving cancellations in quantum field theory amplitudes that could cause the Higgs mass to be much higher than the 125 GeV/c^2 recently observed [11, 12]. The neutralino is a coherent quantum state formed from the SUSY partners of the photon, the Z^0, and Higgs boson H^0, and is a "Majorana" particle, meaning it is its own antiparticle.

Astrophysical measurements show that dark matter behaves like a particle and not like a modification of gravity. Gravitational lensing of distant galaxies by foreground galactic clusters can provide a map of the total gravitational mass, showing that this mass far exceeds that of ordinary baryonic matter. By combining the distribution of the total gravitational mass (from lensing) with the distribution of the dominant component of baryonic matter (evident in the X-ray-emitting cluster gas) one can see whether the dark mass follows the distribution of baryonic matter. For a number of galaxy clusters, in particular the Bullet cluster [13], the total gravitational mass (dominated by dark matter) follows the distribution of other non-interacting test particles (stars) rather than the dominant component of baryonic matter in the cluster gas. Combining this evidence with other observations of stellar distributions and velocity measurements for galaxies with a wide range of mass-to-light ratios, it appears that the total gravitational mass does not follow the distribution of baryonic matter as one would expect for modified gravity, but behaves like a second, dark component of relatively weakly interacting particles.

There are three complementary signals of WIMP dark matter. The dark matter of the Milky Way can interact with atomic nuclei, resulting in NRs that are the basis of direct detection (DD) experiments like LZ. At the LHC, the dark matter should be produced as a stable, non-interacting particle that appears as missing energy and momentum. Out in the cosmos, dark matter collects at the centers of galaxies and in the sun, where pairs of dark matter particles will annihilate with one another, if the dark matter is a Majorana particle, as expected in SUSY theories. The annihilations will produce secondary particles, including positrons, antiprotons, neutrinos, and gamma rays, providing the basis for "indirect" detection (ID) by gamma ray, cosmic ray, and neutrino telescopes.

In Figure 1.1.1, we show the results of a recent analysis of the complementarity of the three signals from WIMP dark matter. The LHC has already provided constraints on the simplest SUSY parameter space, and the Higgs mass is in some tension with the most constrained versions of SUSY, requiring theorists to relax simplifying assumptions. One slightly less restrictive choice of parameters is the so-called phenomenological minimal supersymmetric standard model (pMSSM) model [14, 15]. In Figure 1.1.1, each point represents a choice of pMSSM parameters that satisfies all known physics and astrophysics constraints [10]. The color of the points show which experiments have adequate sensitivity to test whether that point is valid. The black curve shows the expected LZ sensitivity based on an early (2013) LZ estimate, weakened by a factor of four. The three experimental tests are: DD with the proposed LZ experiment, current LHC data, and ID from a proposed ID experiment; an enhanced version of the Cherenkov Telescope Array[16] with twice the number of telescopes compared with the current baseline. Each of the three experimental techniques tends to be most sensitive to one region in Figure 1.1.1, although there are regions of overlapping sensitivity.

The most important goal for the G2 program is to produce the best constraints over the natural mass range for dark matter. The LZ experiment accomplishes this goal. A broader goal of dark matter research is to use the three complementary approaches to establish the validity of any signal, and to identify the properties of the dark matter particle.

1.1.2 Direct Detection Experiments

The direct detection of dark matter in earth-bound experiments depends on the local properties of the Milky Way's dark matter and on the properties of the dark matter particles themselves. The local properties of the Milky Way's dark halo are determined by astrophysical studies, and include the local dark matter mass density as well as the distribution of the velocities of dark matter particles. The conjecture that the dark matter particles are WIMPs implies that their scattering with nuclei is non-relativistic two-body scattering; in LZ, we seek to observe the xenon nuclei that recoil after having been struck by an incoming WIMP. The mass assumed for the WIMP determines the kinematics of the scattering, and the rate of WIMP-nucleus scatters seen in a WIMP detector further depends on the exposure defined as the product of the target mass and the live time, the WIMP-nucleus cross section, and the energy threshold for detection of the NR.

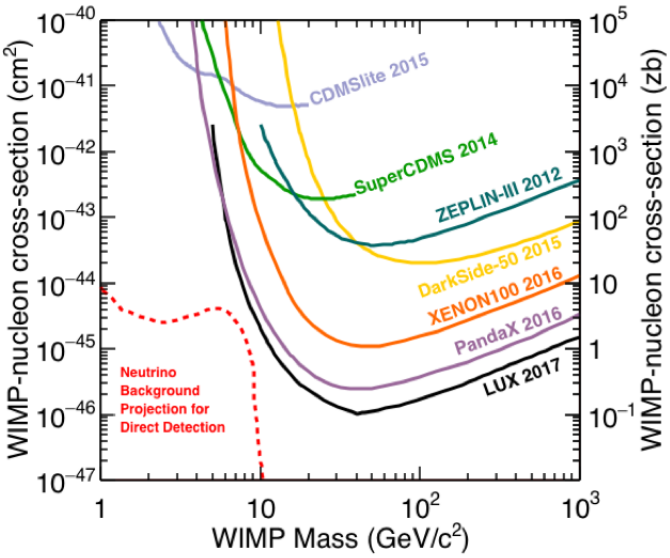

Figure 1.1.2: A compilation of current WIMP-nucleon SI cross-section upper limits at 90 %CL confidence level (solid colored curves, labeled by experiment names). The dotted region at the lower left indicates the region where solar neutrinos contribute background.

The dark matter halo of the Milky Way is harder to quantify than that of other galaxies. The density of all matter, including dark matter, in galaxies is quantified with rotation curves, which describe the average circular velocity of matter in orbit about the galactic center as a function of radius from the galactic center. The rotation curve of the Milky Way for radii larger

than 8.0 kpc, that of our sun, is a challenge to quantify. Estimates of the local dark matter density range from $(0.235 \pm 0.030)\,\mathrm{GeV/cm^3}$ to $(0.389 \pm 0.025)\,\mathrm{GeV/cm^3}$ [17–19]. Most DD experiments adopt, for ease of inter-comparison, a standard value for the local dark matter mass density of $\rho_0 = 0.3\,\mathrm{GeV/cm^3}$. The experiments also adopt a standard distribution function for the velocity of dark matter particles, characterized by a Maxwell-Boltzmann distribution with solar circular velocity $v_0 = 220\,\mathrm{km/s}$, which is cut off at the galactic escape velocity of $v_{esc} = 544\,\mathrm{km/s}$, and with proper accounting for the sun's peculiar velocity and the periodic annual motion of the Earth [20, 21]. The minimum WIMP mass detectable with a particular DD experiment depends on the maximum velocity in the galactic WIMP spectrum, the atomic mass A of the target nucleus, and the energy threshold E_{min} for NR detection in that experiment. Straightforward kinematics gives the minimum detectable WIMP mass as $M_{WIMP}(\mathrm{GeV}) \approx (1/4)\sqrt{E_{min}(\mathrm{keV})A}$ for a maximum velocity of v_{esc} = 544 km/s. This minimum M_{WIMP} is 1.6 GeV for the recent CDMSlite Ge-target result [22], and 4 GeV for the recent LUX result [23] using LXe.

These results are shown in Figure 1.1.2, along with the current experimental situation for the spin–independent (SI) WIMP-nucleon cross section. We discuss the details of spin independence and other types of WIMP-nucleon interactions in Chapter 2. The SI cross section is the standard benchmark, and would result from a WIMP coupling to the Standard Model Higgs. As the presumed M_{WIMP} rises above this value, the portion of the WIMP velocity distribution function that permits NR above the detectable threshold rises rapidly. This rapid rise drives the improvement in sensitivities as M_{WIMP} rises above 5 GeV, as shown in Figure 1.1.2. As M_{WIMP} approaches the mass of the atom used in the target, the kinematics of energy transfer to the target nuclei becomes most efficient, and experiments reach their maximum sensitivity.

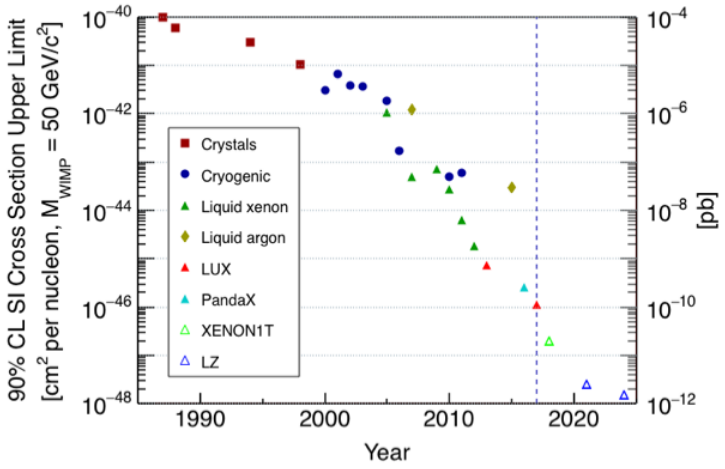

Figure 1.1.3: The evolution of cross-section limit for 50-GeV WIMPs as a function of time. Past points are published results. Future points are from the Snowmass meetings [24].

This region, with $M_{WIMP} > 10\,\mathrm{GeV}$ roughly, is the region most likely for a WIMP, as other weak-interaction particles, including the Z^0, the W, and the Higgs particles, have masses in that region. As E_{min} grows yet larger, the number density of WIMPs implied by the astrophysical mass density, $\rho_0 = (0.3\,\mathrm{GeV}/M_{WIMP})/\mathrm{cm^3}$ falls, reducing the sensitivity of direct-detection experiments, as shown in Figure 1.1.2. The maximum WIMP mass consistent with thermal equilibrium in the early universe is $340\,\mathrm{TeV}/c^2$, above which unitarity can no longer be satisfied [25].

The history of and future projections for WIMP sensitivity are shown in Figure 1.1.3. There are three distinct eras: (1) 1986-1996; (2) 2000-2010; and (3) post-2010. In the first era, low-background Ge and NaI crystals dominated. In these experiments, discrimination between the dominant background of electron recoils (ERs) from gamma rays and NRs was not available. The cross-section sensitivity per nucleon achieved, $10^{-41}\,\mathrm{cm^2}$, was sufficient to rule out the most straightforward WIMP implementation: that the WIMP is a heavy Dirac neutrino, which was the original suggestion of Ref. [9]. In the second era, cryogenic Ge detectors with the ability to distinguish NR from the ER background dominated, and achieved a cross-section per nucleon sensitivity of $5 \times 10^{-44}\,\mathrm{cm^2}$. This sensitivity began to probe dark matter

that is a Majorana fermion, which couples to nucleons via the Higgs particle. In the third era, still under way, LXe time projection chambers (TPCs) have been most sensitive, and with the LUX experiment have achieved an upper limit for the WIMP-nucleon spin-independent cross section of 1.1×10^{-46} cm^2(=1.1×10^{-10} pb) [26]. The LXe TPC has the ability to discriminate ER and NR, and can be expanded to large, homogeneous volumes. It is possible to make accurate predictions for the backgrounds in the central LXe TPC region, particularly with the added power of outer detectors that can characterize the radiation field in the TPC vicinity.

A more detailed portrayal of the variety of experiments, both from the past and projected into the future, is given in Figure 1.1.4 [24]. In the region $M_{\mathrm{WIMP}} > 10\,\mathrm{GeV}/c^2$, most likely for a WIMP due to proximity to the masses of the weak bosons, LZ will be the most sensitive experiment. Figure 1.1.4 also shows the "neutrino floor", where NRs from coherent neutrino scattering, a process that has not yet been observed, will greatly influence progress in sensitivity to WIMP interactions. A 1,000-day run of the LZ experiment will just begin to touch this background. Searches for direct interactions of dark matter with exposure substantially greater than LZ will see many candidate events from NRs in response to, primarily, atmospheric neutrinos.

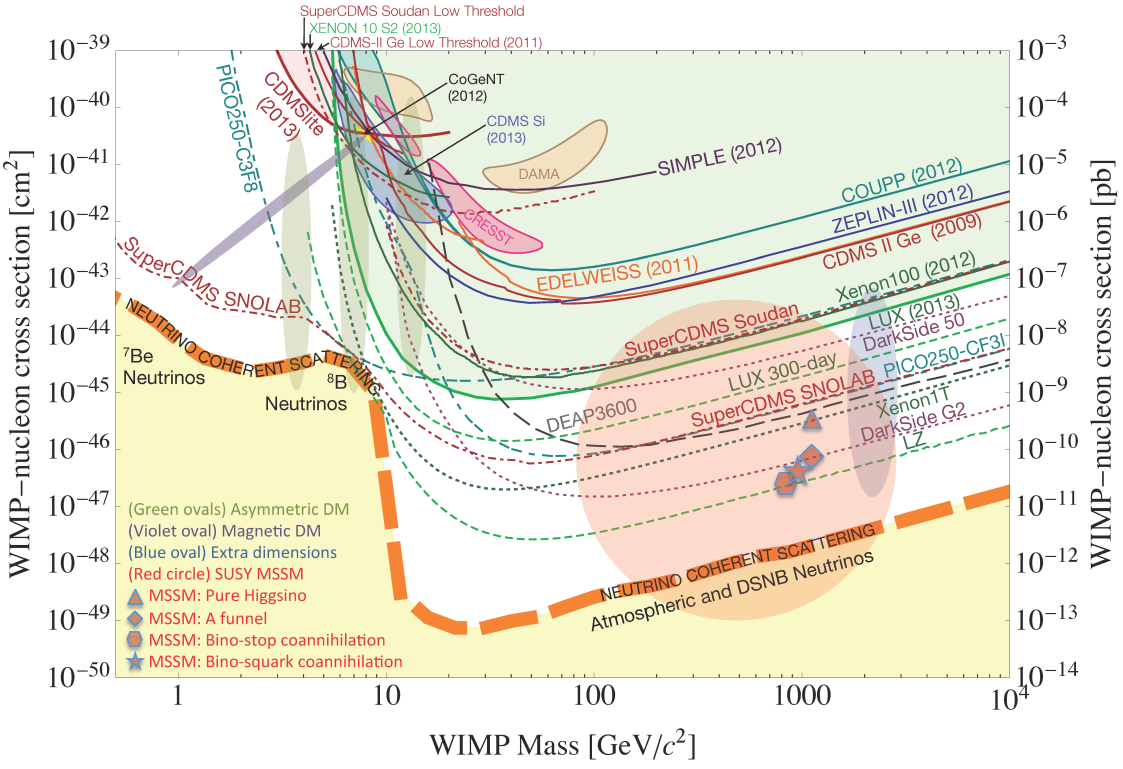

Figure 1.1.4: A compilation of WIMP-nucleon SI cross-section sensitivity (solid curves), hints for WIMP signals (shaded closed contours), and projections (dot and dot-dash curves) for DD experiments of the past and projected into the future. This figure captures the experimental situation as of the end of 2013 and was reported in the 2013 Snowmass CF1 summary. Also shown is an approximate band where the coherent nuclear scattering of ^{8}B solar neutrinos, atmospheric neutrinos, and diffuse supernova neutrinos will limit the sensitivity of DD experiments to WIMPs. Finally, a suite of theoretical model predictions is indicated by the shaded regions, with model references included [24].

1.2 Instrument Overview

The core of the LZ experiment is a two-phase xenon (Xe) time projection chamber (TPC) containing 7 fully active tonnes of LXe. Scattering events in LXe create both a prompt scintillation signal (S1) and free electrons. Electric fields are employed to drift the electrons to the liquid surface, extract them into the gas phase above, and accelerate them to create a proportional scintillation signal (S2). Both signals are detected by arrays of photomultiplier tubes (PMTs) above and below the central region. The difference in time of arrival between the signals measures the position of the event in z, while the x, y position is determined from the pattern of S2 light in the top PMT array. Events with an S2 signal but no S1 are also recorded. A 3-D model of the LZ detector located in a large water tank is shown in Figure 1.2.1. The water tank is located at the 4,850-foot level (4850L) of the Sanford Underground Research Facility (SURF). The heart of the LZ detector (including the inner titanium [Ti] cryostat) will be assembled on the surface at SURF, lowered in the Yates shaft to the 4850L of SURF, and deployed in the existing water tank in the Davis Cavern (where LUX is currently located). The LZ experiments principal parameters are given in Table 1.2.1, along with the Work Breakdown Structure (WBS) for the LZ Project.

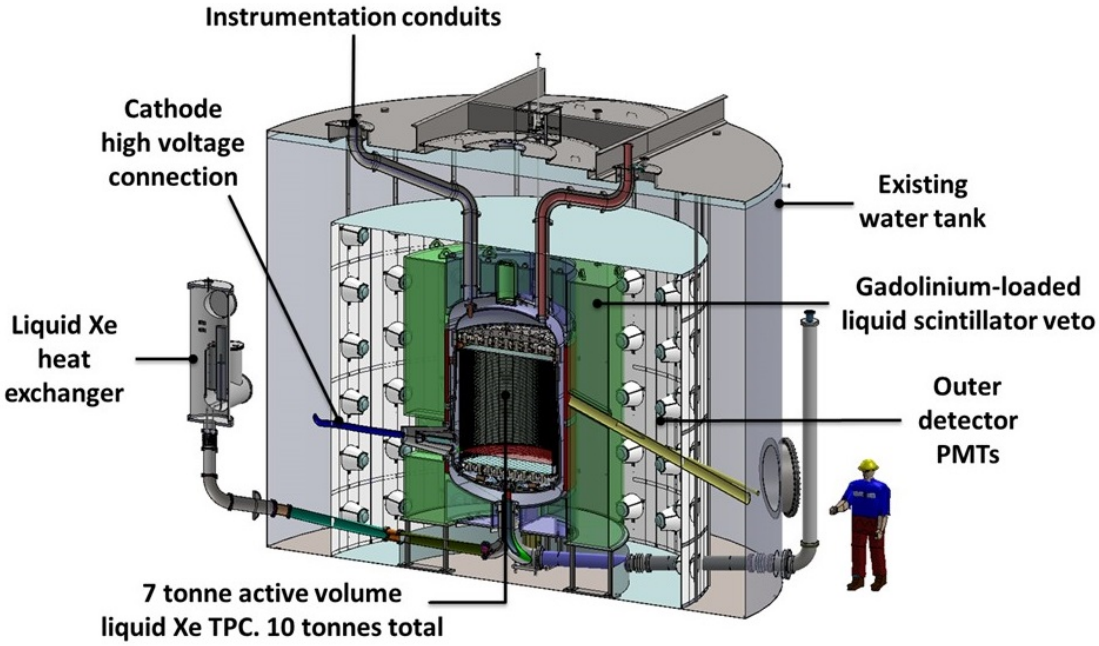

Figure 1.2.1: The LZ detector concept.

The LZ detector includes several added capabilities beyond the successfully demonstrated LUX and ZEPLIN designs. The most important addition is a nearly hermetic liquid organic scintillator (gadolinium-loaded linear alkyl benzene [LAB]) outer detector, which surrounds the central cryostat vessels and the TPC. The outer detector and the active Xe "skin" layer, the Xe between the inner cryostat wall and the outer wall of the TPC, operate as an integrated veto system, which has several benefits. The first is rejecting gammas and neutrons generated internally (e.g., in the PMTs) that scatter a single time in the fully active region of the TPC and would otherwise escape without detection; this could mimic a weakly interacting massive particle (WIMP) signal. As these internally generated backgrounds interact primarily at the outer regions of the detector, the veto thus allows an increase in the fiducial volume.

Table 1.2.1: Principal parameters of the LZ detector organized to reflect the responsible work package under the Work Breakdown Structure (WBS).

WBS	Description	Quantity
1.1	**Xenon Procurement**	
	Approximate total mass	10 tonnes
	Mass inside TPC active region	7 tonnes
	Approximate fiducial mass	5.6 tonnes
1.2	**Xe Vessel(Cryostat)**	
	Inner cryostat—inside diameter (tapered), height, wall thickness	1.58 —1.66 m, 2.59 m, 8 —11 mm
	Outer cryostat—inside diameter, height, wall thickness	1.83 m, 3.04 m, 7 —14 mm
	Approximate cryostat weights—inner, outer	0.95 tonne, 1.12 tonne
1.3	**Cryogenic System**	
	Cooling power	1 kW @ 80 K
	Input electrical power	11 kW
1.4	**Xenon Purification**	
	Krypton content	<0.015 ppt (g/g)
	Allowed air content (Kr equivalent)	<40 cc
	^{222}Rn content in active Xe	<2 µBq/kg
	Recirculation rate	500 slpm
	Electron lifetime	>0.8 ms
	Charge attenuation length	>1.5 m
1.5	**Xenon Detector**	
	Top (Bottom) TPC 3-inch PMT array	253 (241), 494 total tubes
	"Side skin" PMT and "dome" PMT	113 and 18, 131 (93 1-inch,38 2-inch) total
	Nominal (Design) cathode operating voltage	50 (100) kV
	Reverse field region (cathode to bottom tube shield)	0.1375 m
	TPC height (cathode to gate grid)	1.456 m
	TPC effective diameter	1.456 m

(continued on next page)

Table 1.2.1: (continued)

WBS	Description	Quantity
1.6	**Outer Detector System**	
	Weight of Gd-loaded LAB scintillator	17.5 tonnes
	Number of acrylic vessels, total acrylic mass	9 vessels, 3.1 tonnes
	Number of 8-inch PMTs	120
	Minimum thickness of scintillator	0.61 m
	Diameter of water tank	7.62 m
	Height of water tank	5.92 m
	Approximate weight of water	228 tonnes
1.7	**Calibration System**	
	Number of source deployment tubes	3
	Number of neutron tubes	3
	Other calibration tools	^{83m}Kr, n-generator, tritiated CH_4 , ^{37}Ar, ^{m}Xe
1.8	**Electronics, DAQ, Controls, and Computing**	
	Trigger rate (all energies, 0 keV to 40 keV)	40 Hz, 0.4 Hz
	Average event size (noncalibration, uncompressed)	0.2 MB to 1.0 MB
	Data volume per year	350 TB to 850 TB
1.9	**Integration and Installation**	
1.10	**Cleanliness and Screening**	
1.11	**Offline Computing**	
1.12	**Project Management**	

Additionally, this direct vetoing is an important means of risk mitigation against one of the detector components (e.g., the cryostat materials or the PMTs) having a higher-than-expected background. A second benefit of the outer detector is that the combination of outer detector and segmented Xe detector will form a nearly hermetic detection system for all internal radioactivity. This will not only directly measure the internal backgrounds with a very high level of detail and completeness, but also help provide an understanding of the detectors response to those backgrounds that can be included in our analysis for dark matter signals.

As shown in Figure 1.2.1, the liquid scintillator volume is confined in segmented, clear acrylic vessels encapsulating the Ti cryostat of the central LZ detector. PMTs mounted on ladders in the outer water shield simultaneously view the light from both the scintillator and inner water volumes. The design of the acrylic vessels is advanced and industrial fabrication of the vessels has started. The production of the low-radioactivity

liquid scintillator is based on the successful production of a similar scintillator for the Daya Bay experiment, albeit with lower backgrounds. The layer of LXe located between the PTFE (polytetrafluoroethylene, or Teflon®) structure that surrounds the fully active region and the cryostat wall, as well as the LXe region beneath the bottom PMT array forms the "skin" element of the veto system. A skin of some (∼few cm, more in the bottom region of the detector) thickness is difficult to avoid given the TPC geometry, the need for high-voltage (HV) standoff, and the strong mismatch in thermal expansion between the PTFE panels and Ti vessels. The skin readout alone has a limited veto efficiency, but has sufficient gamma-stopping power to augment the scintillator veto. The combination of skin readout and outer detector creates a highly efficient integrated veto system. Scintillation light from the skin region is observed by a sparse PMT array dedicated to this region. Thin PTFE panels are attached to the inner cryostat wall and bottom (dome) region to enhance light collection.

For detector calibration, neutron and gamma-ray sources will be brought next to the wall of the inner cryostat via an array of three source tubes that penetrate the water and organic scintillator. The principal calibrations, metastable krypton and xenon and tritiated methane, will be introduced directly into the LXe via the Xe gas-handling system to allow in situ calibration. An external neutron generator that produces neutrons through a deuterium-deuterium fusion reaction will also be employed, and the neutrons penetrate through the water and scintillator veto through dedicated tubes. Additional neutron calibration sources will also be employed.

Another key determinant of the sensitivity of the experiment is the level of discrimination of electron recoil (ER) backgrounds from nuclear recoils (NRs). This depends on the electric field established in the TPC. The nominal operating voltage (cathode-to-anode) is 50 kV but all components will be designed to a voltage of 100 kV (and in general tested to higher voltages) to have sufficient operating margin.

The LZ TPC detector will employ Hamamatsu R11410-20 3-inch-diameter PMTs with a demonstrated low level of radioactive contamination and high quantum efficiency. Materials for these PMTs have been procured and screened to demonstrate low radioactivity. Tube production and testing began in 2016. Care will be taken in the design of the highly reflective PTFE TPC structure to isolate light produced in the central volume from the skin region, and vice-versa. Additional 1-inch PMTs will be utilized in the cylindrical skin region as well as a few 2-inch tubes (from LUX) and 2-inch tubes used in the dome region.

The design of TPC mechanical and HV systems is advanced. Small prototypes of the high-electric field region of the TPC have been fabricated and tested in liquid argon (LAr) and successfully in a LXe test facility at SLAC National Accelerator Laboratory (SLAC). A scaled-prototype of the TPC and all grids that shape the electric fields is being tested at SLAC. HV systems, including the cathode HV delivery system, will be tested in LAr at LBNL in a dedicated facility. Assembly of the TPC structures and HV elements will occur primarily at LBNL-SLAC. The low-radioactivity Ti mechanical supports for the 3-inch PMTs will be industrially manufactured and the PMTs loaded and tested at Brown University.

LZ will employ an array of liquid nitrogen (LN)-cooled thermosyphons to control the detector temperature and minimize thermal gradients. The purification system is a scaled-up version of the LUX room-temperature gas-phase purification system, and will exploit the liquid/gas heat-exchanger technology developed for LUX to minimize LN consumption. A cryocooler will be used underground to manufacture LN, and LN storage vessels used by LUX will be retained as backup. The Xe circulation and purification system is similar conceptually to that used in LUX but with a much higher capacity. The 10 tonnes of Xe will be circulated and purified in 2 to 3 days. The Xe purity will be monitored carefully by a dedicated system, expanding and improving on a similar system used in LUX. Radon will be removed from selected regions of the detector that contain Xe gas using a dedicated system underground, to lower the radon content.

The acquisition of the 10 tonnes of Xe has started. The Xe used in LUX and in other devices will be reused. Procurement began in 2015 and is planned to end by mid-2018. All gaseous Xe is to be delivered

to SLAC, where krypton will be removed through a chromatographic process using scaled-up techniques already demonstrated successfully for LUX.

The electronics front-end, trigger and data acquisition, and slow controls are based on the LUX experience but will be significantly expanded and improved. A test of the PMT analog-amplifier-digitizer system, with full cable lengths, has been successfully completed. In addition, a few PMTs in the LUX experiment were operated successfully with prototype electronics systems after the completion of LUX data taking in mid-2016. Software and computing systems for LZ are based on the successful operation of LUX, analysis of LUX data, and the experience of other experiments at LBNL and collaborating institutions. LZ data will be buffered locally at SURF and then transmitted to primary data storage at LBNL that will be mirrored in the U.K. The analysis framework to be used by the LZ collaboration has been defined and the simulation of the LZ detector and its response is already well advanced. The results are given in other chapters of this Technical Design Report.

Components of LZ will be manufactured at a number of locations and brought to SURF. Assembly of the Xe detector and the inner cryostat will occur in a dedicated and upgraded cleanroom at SURF that includes an augmented air handling system to reduce radon during the assembly process. The construction of the facilities to house the upgraded cleanroom began in September 2016. The reduced-radon air handling system is under construction as is a reduced-radon cleanroom. Work on improved surface facilities will be completed by mid-2017. A comprehensive system for tracking components, ensuring cleanliness and a very low dust environment, will be employed to minimize radioactive backgrounds. The inner cryostat with the Xe detector inside will be lowered as a unit down the Yates shaft and transported to the Davis Cavern water tank. Another system will be built underground to provide low-radon air to the water tank during the connection of the inner cryostat to other systems and for other uses. All other components will be staged at SURF, lowered via the Yates shaft, and similarly transported. This includes the segmented acrylic vessels for the outer detector system and other large components. The gaseous Xe will be stored in specially designed cylinders in a dedicated room underground close to the Davis Cavern.

1.3 Design Drivers for WIMP Identification

Having established the motivation to perform direct searches for WIMP dark matter, we introduced in the previous section the configuration of LZ. Searching for events that are rare ($\lesssim$0.1 /t/d) and that involve very small energy transfers ($\lesssim$100 keV) is extremely challenging. This section focuses on the more salient features of the experiment and the detection medium, and how these will contribute to the identification of a galactic WIMP signal with low systematic uncertainty. The detailed design and its technical implementation are described in later sections; here, we address the key requirements that drive the technical design.

1.3.1 Overview of the Experimental Strategy

Xenon has long been recognized as a very attractive WIMP target material [27–29]. Its high atomic mass provides a good kinematic match to intermediate WIMP masses of O(100 GeV/c^2) and the largest spin-independent scattering cross section among the available detector technologies, as illustrated in Figure 1.3.1. Sensitivity to lighter WIMPs, with masses of O(10 GeV/c^2), can be also be achieved, given the excellent low-energy scintillation and ionization yields in the liquid phase [30]. Xenon contains neither long-lived radioactive isotopes with troublesome decays nor activation products that remain significant after the first few months of underground deployment. It is also sensitive to spin-dependent interactions via the odd-neutron isotopes ^{129}Xe and ^{131}Xe, which account for approximately half of the natural isotopic abundance. If a WIMP discovery were made, the properties of the new particle could be studied by altering the isotopic composition of the target. This broad WIMP sensitivity confers maximum discovery potential to LZ.

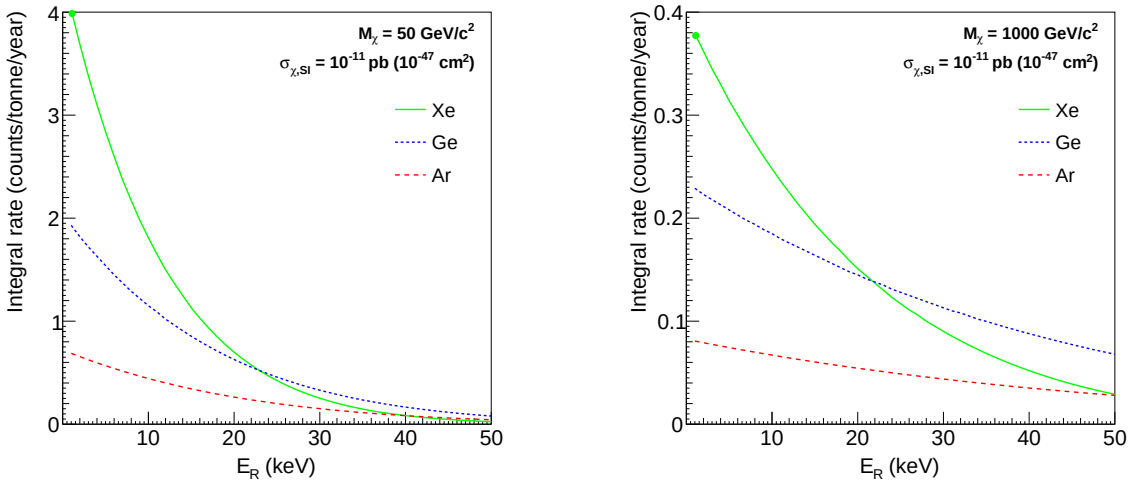

Figure 1.3.1: Integrated rate above threshold per tonne-year of exposure for WIMP elastic scattering on Xe, Ge, and Ar targets for 50 GeV/c^2 and 1 TeV/c^2 WIMP masses and 10^{-47} cm^2 interaction cross section per nucleon. The green marker indicates the 1.1 keV$_{nr}$ WIMP-search threshold in LUX with nominal ER/NR discrimination [30]. CDMS II searched above ~5 keV in their Ge target [31]; selected SuperCDMS detectors allowed a 1.6 keV$_{nr}$ threshold with lower discrimination [32]; CDMSlite search for low-mass WIMPs with an electron recoil threshold down to 56 eV [22]. In LAr, the DarkSide-50 experiment has recently conducted a WIMP search above 13 keV$_{nr}$ [33].

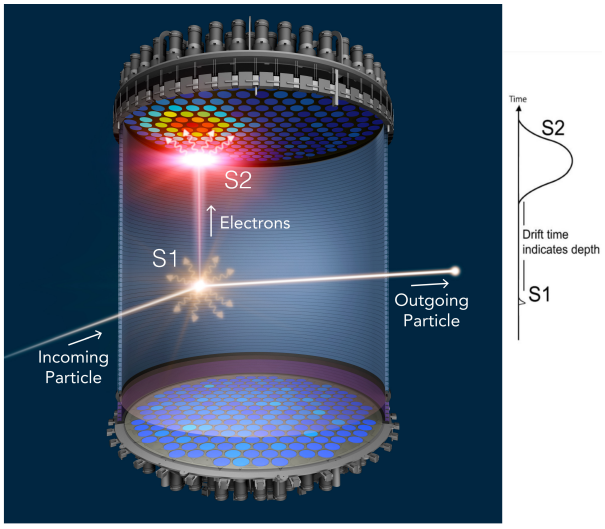

Figure 1.3.2: Operating principle of the double-phase Xe TPC. Each particle interaction in the LXe (the WIMP target) produces two signatures: one from prompt scintillation (S1) and a second, delayed one from ionization, via electroluminescence in the vapor phase (S2). This allows precise vertex location in three dimensions and discrimination between nuclear and electron recoils.

The liquid phase is preferred over the gas phase due to its high density (3 g/cm^3) and high scintillation yield, and because its charge quenching of NRs provides a powerful particle ID mechanism. Early experiments such as ZEPLIN-I [34] exploited simple pulse shape discrimination (PSD) of the scintillation signal to reject electronic backgrounds; however, this achieved modest rejection efficiencies and only at relatively high recoil energies. When the first double-phase Xe detectors were deployed for dark matter searches, in the ZEPLIN-II/III [35, 36] and XENON10 [37] experiments, the increase in engineering complexity soon paid off in sensitivity, and this technique has been at the forefront of the field ever since. Comprehensive reviews on the application of the noble liquids to rare-event searches can be found in the literature [38, 39].

The TPC configuration at the core of double-phase detectors, illustrated in Figure 1.3.2, has several notable advantages for WIMP searches, in that two signatures are detected for every interaction: a prompt scintillation signal (S1) and the delayed ionization response, detected via electroluminescence in a thin gaseous phase above the liquid (S2). These permit precise event localization in three dimensions (to within a few mm [40]) and discrimination between electron and nuclear recoil events (potentially reaching 99.99 % rejection [41]).

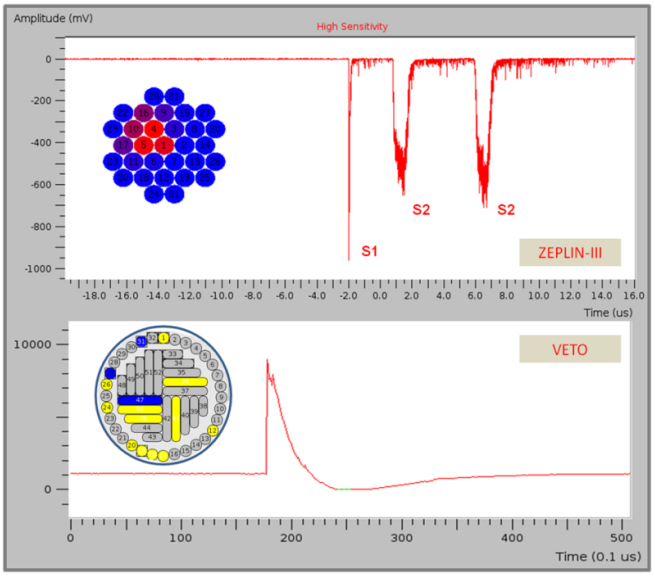

Figure 1.3.3: A double-scatter neutron event recorded in ZEPLIN-III. The upper panel shows two elastic vertices clearly resolved in drift time (two S2 pulses, representing different vertical coordinates), although both have similar horizontal positions. The lower panel shows the summed waveform from the 52-module veto detector which surrounded the main instrument, indicating radiative capture of this neutron some 17 µs after interacting in the LXe target. Recording additional particle scatters (either in the WIMP target or in an ancillary veto detector) provides a powerful rejection of backgrounds.

Both channels are sensitive to very low NR energies. The S2 response enables detection of single ionization electrons extracted from the liquid surface due to the high photon yield that can be achieved with proportional scintillation in the gas [42–44]. In LUX we have demonstrated sufficient S1 light collection to achieve a NR energy threshold below 1.1 keV$_{nr}$ [45]. The combination of accurate 3-D imaging capability within a monolithic volume of a readily purifiable, highly self-shielding liquid is nearly an ideal architecture for minimizing backgrounds. It allows optimal exploitation of the powerful attenuation of external gamma rays and neutrons into LXe, distinguishes multiply-scattered backgrounds from single-site signals, and precisely tags events on the surrounding surfaces. This latter feature is important, given the difficulty of achieving contamination-free surfaces. The low surface-to-volume ratio of the large, homogeneous TPC lowers surface backgrounds in comparison to signal, and stands in stark contrast to the high surface-to-volume ratio of segmented detectors.

These concepts are illustrated in Figure 1.3.3, which shows neutron interactions occurring just a few millimeters apart in the ZEPLIN-III detector. The S1 signals are essentially time-coincident, but the S2 pulses have different time delays corresponding to different vertical coordinates, making the rejection of such multiple scatters extremely efficient. The figure

shows also a pulse observed in delayed coincidence in the surrounding veto detector, indicating radiative capture of this neutron on the gadolinium-loaded plastic installed around the WIMP target. LZ will utilize a similar anticoincidence detection technique to characterize the radiation environment around the Xe detector and to further reduce backgrounds.

Nevertheless, when the first tonne-scale Xe experiments were proposed just over a decade ago, it was unclear whether LXe technology could be monolithically scaled as now proposed for LZ, or if it would be necessary to replicate smaller devices with target masses of a few hundred kilograms each. The latter option, while conceptually simple, fails to fully exploit the power of self-shielding. Since then, several aspects of the double-phase TPC technique have been further developed to make LZ technologically feasible. First, the ionization and scintillation yields of LXe and their dependence on energy, electric field, and particle type have now been established down to a few keV by a comprehensive development program carried out around the globe, including substantial work by members of the LZ Collaboration. Second, good acceptance for the primary scintillation light must be maintained as the detector becomes larger, and the remarkably high reflectance >95 % of PTFE at the 178 nm LXe scintillation wavelength has made this practical. Third, considerable control over electronegative impurities is required to drift charge over a distance of a meter or more, and commercial purification technology and new screening and detection methods developed by LZ scientists have made this routinely achievable. Fourth, the extraordinary self-shielding of an LZ-class instrument requires the use of internal calibration sources, and these have now been developed and deployed within LUX by LZ groups. Fifth, radioactive impurities such as Kr must be reliably removed from the Xe, and other sources of internal radioactivity such as radon must be tightly controlled. Finally, a large detector requires a substantial cathode voltage, or else fluctuations in the charge recombination near the interaction site will degrade the recoil discrimination. Very recently, LUX has demonstrated a rejection efficiency of 99.6 % (for 50 % NR acceptance) even at a modest field of 180 V/cm [30], matching already the baseline assumption for LZ.

On the whole, the progressive nature of our program has contributed to an increase in the readiness level of this technology: LZ entails a twentyfold scale-up from LUX, the latter being also an order of magnitude or so larger than the ZEPLIN and XENON10 targets. Besides having the favorable properties of the WIMP target material and the proven sensitivity of the technology to small energy deposits, a successful experiment must achieve very low background rates over a significant fraction of its active medium. Indeed, it is worth noting that LZ will be a factor of 10^4 times more sensitive than current limits from the EDELWEISS and Cryogenic Dark Matter Search (CDMS) experiments, which led in sensitivity only one decade ago [46, 47]. This implies a corresponding reduction in the background rate. This is achieved to first order by the power of self-shielding of local radioactivity, in combination with an outer layer of instrumented LXe and a hermetic gadolinium-loaded scintillator "veto" shield capable of tagging neutrons and gamma rays with high efficiency. The construction of a veto instrument at the required scale builds on two decades of development work in the field of reactor neutrino physics, and its development within LZ is led by scientists with considerable expertise in this area. Three other important developments, again pioneered by LZ groups, have also made this possible: the development, in collaboration with Hamamatsu, of very-low-background PMTs compatible with LXe [48]; the identification via the LUX program and LZ R&D program of radio-clean titanium for cryostat fabrication [49, 50]; and the development of krypton-removal and -screening technology capable of delivering sub-ppt concentrations [51, 52].

This strategy leads to a WIMP-search background of order 6 events in 1,000 days of live exposure for a 5.6-tonne fiducial mass. The remaining component is dominated by events from radon decay in the fiducial volume, a small fraction of which mimic NRs due to the finite S2/S1 discrimination power. Coherent scattering of atmospheric neutrinos from Xe nuclei (CNS) will constitute an even smaller, but irreducible, background. These rates are well understood and background expectations are calculable with small system-

atic uncertainty (e.g., these events are spatially uniform and their energy spectra are well known). With its pioneering capability, LZ will be sensitive to these ultra-rare processes.

1.3.2 Self-shielding in Liquid Xenon

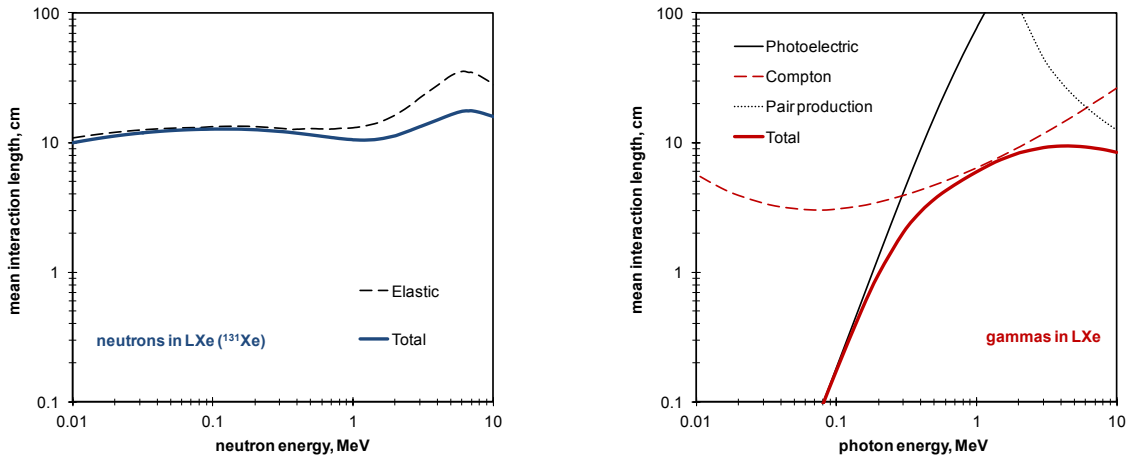

Figure 1.3.4: Mean interaction lengths for neutrons [53] and gamma rays [54] in LXe.

At the core of any WIMP search experiment is a substantial screening and materials-selection program (Chapter 9) that controls the trace radioactivity of the detector components. In the case of LZ, however, backgrounds from detector radioactivity will also be rejected to unprecedented levels by the combination of self-shielding of external particles and operation in anticoincidence with outer veto detectors (Chapter 4). This will render external gamma rays and neutrons less problematic than in other experiments.

The self-shielding strategy, in particular, relies on the combination of a large, dense, high-Z and continuous detection medium with the ability to resolve interaction sites in three dimensions with high precision. An outer layer of the target can therefore be defined (in data analysis) that shields a fiducial region with extremely low background at the center of the active medium. The nonfiducial layer will be only a few centimeters thick. Because the size of the LZ detector is much larger than the interaction lengths for MeV gamma rays and neutrons, as shown in Figure 1.3.4, when these particles penetrate more than a few cm they will scatter multiple times and be rejected (Figure 1.3.5). X-rays, with energies similar to WIMP events, penetrate only a few mm into the LXe.

Double-phase Xe detectors implement this strategy very successfully, and this is reflected in their present dominance in WIMP sensitivity—with LUX being a prime example of this concept. In LZ, a fiducial mass of nearly 6 tonnes will be practically free of external gamma-ray or neutron backgrounds, which represents 85 % of active mass within the TPC, compared to about 50 % for LUX [30] and XENON100 [55]. In addition to the required high density and high-Z of the detection medium, we highlight the importance of the precise spatial resolution that can be achieved in these detectors, which is of the order of 1 cm or better at threshold.

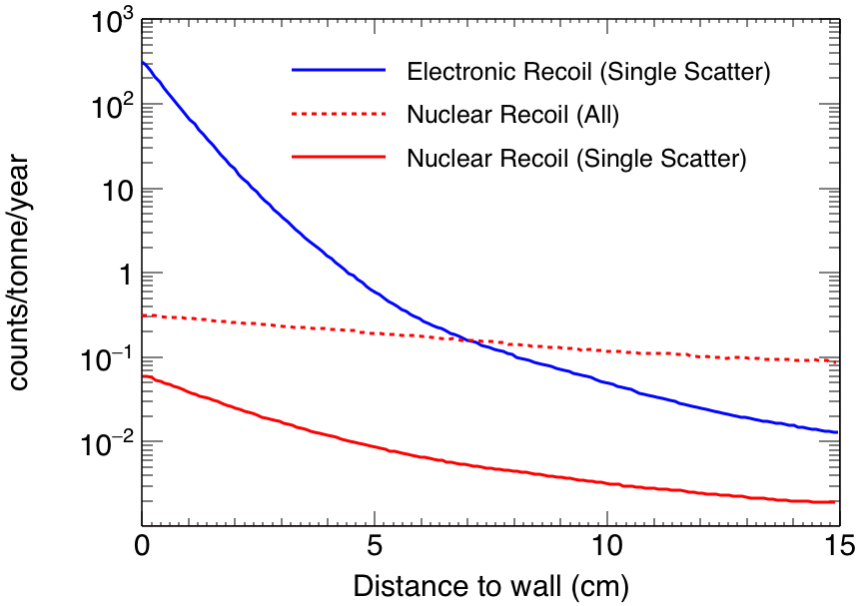

Figure 1.3.5: Self-shielding of external neutrons and gamma rays in LXe. The red lines indicate the number of elastic neutron scatters creating 6 keV_{nr} to 30 keV_{nr} NRs as a function of distance to the lateral TPC wall; the continuous line shows single scatters only, while the dashed line includes all multiplicities adding up to the same total energy; the input spectrum is that from (α,n) neutron production in PTFE, an important background near the TPC walls. The blue line represents single-site ER interactions from U/Th gamma rays from PTFE with energy 1.5 keV_{ee} to 6.5 keV_{ee}. A tenfold decrease is achieved at ≈2 cm and ≈6 cm from the wall for gamma rays and neutrons, respectively.

1.3.3 Low-energy Particle Detection in Liquid Xenon

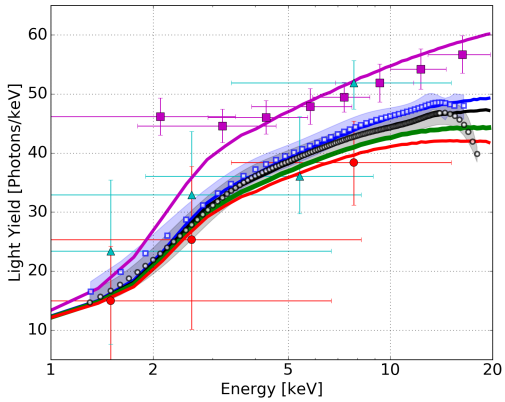

Figure 1.3.6: Absolute ER scintillation yield in LXe. Purple squares are from Compton-scattering measurements at Columbia [56] and cyan triangles from [57] – both at zero field. Blue/black squares/circles are from LUX tritium beta emission measurements in situ at 105 and 180 V/cm respectively [58]. Red circles are from Compton-scattering measurements performed in Zürich at 450 V/cm [57]. The NEST model (updated from [59, 60] but using the same framework and formulae still) is shown in purple, blue, black, green, and red for 0, 105, 180, 310 (LZ baseline), and 450 V/cm, respectively.

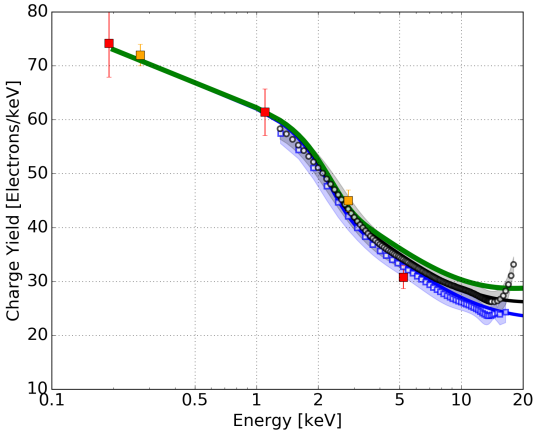

Figure 1.3.7: ER ionization yield in LXe. Data are as follows: blue squares from LUX tritium data beta spectrum matching at 105 V/cm [58]; red and orange squares from ^{127}Xe activation lines in LUX and ^{37}Ar in PIXeY, respectively, all at 180 V/cm [F,G]; black circles from LUX at 180 V/cm once again [58]. The NEST model is shown in blue, black, and green for 105, 180, and 310 V/cm (LZ baseline), respectively. The green curve in each plot is what is used for all of the ER background modeling in LZ. Low-energy beta particles and gamma-rays are treated equivalently as both generating ER in the context of the simulation. Increasing the magnitude of the drift electric field reduces the recombination probability, thus raising the charge yield at the expense of light, as with NR.

The potential of this medium for particle detection was recognized in the mid-20th century, when the combination of good scintillation and ionization properties was first noted (see [38] and references therein). In the 1970s, the first double-phase detectors were demonstrated, originally using argon [61]. Initially, our understanding of the mechanisms involved in generating the scintillation and ionization responses in the noble liquids progressed slowly, especially regarding the response to low-energy nuclear and electron recoils. However, great steps have been taken in the past decade, with LZ collaborators taking a central role. This effort continues around the world.

In this section, we summarize those LXe properties that affect the detection of low-energy nuclear and electronic recoils via scintillation and ionization; the next section discusses how to discriminate between them. The response of LXe to electron and nuclear recoils is now well understood over the energy range of interest for "standard WIMP" searches $\gtrsim$1.1 keV$_{\mathrm{nr}}$ [45]. Significant progress has equally been made in modeling its behavior as a function of incident particle species, energy, and electric field, in order to optimize detector design and the physics analyses. Naturally, the increasing WIMP scattering rates with decreasing recoil energy and the need to probe lighter dark matter candidates mean that pushing further down in threshold is a perennial concern for any detection technology.

Scintillation and ionization yields for ERs in LXe are shown in Figures 1.3.6 and 1.3.7, with predictions by the Noble Element Simulation Technique (NEST) model (see [56, 57, 60] and the brief description in Chapter 12); data for Compton electrons now reach down to 1.5 keV_{ee} [56, 65], and NEST shows good agreement with these results [59]. LXe compares favorably to the best scintillators and is also a good ionization medium. For example, the maximum photon yield at a few tens of keV is some 40 % higher than that of liquid argon. This is important for a number of reasons: It reduces the variance of the ER response, which is important for particle discrimination; it permits effective detector calibration; and it is directly relevant to some leptophilic dark matter searches.

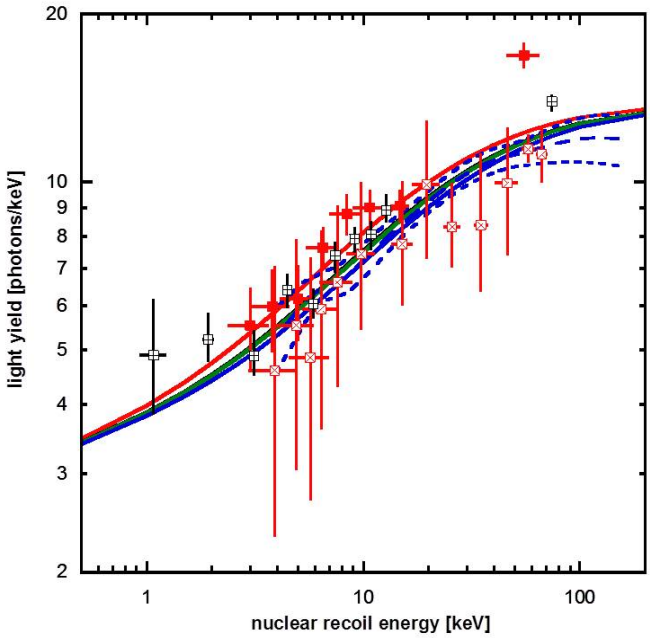

Figure 1.3.8: Absolute NR scintillation yield in LXe. Hollow red markers are from neutron-beam measurements at Yale [62] and filled markers from [63]—both at zero field. Black squares are from LUX D-D neutron gun measurements in situ at 180 V/cm [23]. Blue dashed lines are the combined mean and 1-σ curves from two in situ measurements with Am-Be neutron sources via fitting to MC simulation from ZEPLIN-III [64] (3,650 V/cm). The NEST model (updated from [65] but using the same framework and formulae) is shown in red, black, green, and blue for 0, 180, 310 (LZ baseline), and 3,650 V/cm, respectively. The green curve is used for LZ sensitivity calculations.

As Figure 1.3.6 suggests, the scintillation yield is suppressed with increasing electric-field strength, while the ionization yield improves by the same amount. This behavior is also observed for individual events: A fraction of the photon yield comes from recombination luminescence, whereby VUV photons are generated from electron-ion recombination occurring near the interaction site, and therefore some electrons contribute either to scintillation (S1) or to ionization (S2), but not to both. This event-by-event anticorrelation of the two signatures can be exploited very effectively at higher energies in double-phase detectors to obtain good energy resolution for the spectroscopy of ERs, with application to gamma-ray background studies and searches for $0\nu\beta\beta$ decay.

For NRs, both data and modeling have progressed markedly in recent years. The picture here is more complex than for electron interactions. Most of the energy deposited by electrons is shared between ionization and excitation of the medium, making much of it observable. In NR interactions, a larger fraction is spent in atomic collisions, which is dissipated as heat and not detected. However, data obtained by scattering experiments at neutron beams ex situ, e.g. [62, 63], are now in good agreement with those from indirect in situ techniques [64], down to ~3 keV.

As the NR scintillation yield declines gently at least down to 3 keV, the ionization yield increases accordingly, as shown in Figure 1.3.9, with the current state of the art for in-situ measurement coming from LUX. This measurement, for the first time, constrains the ionization yield below 1 keV (0.7 keV) [23]. We note that

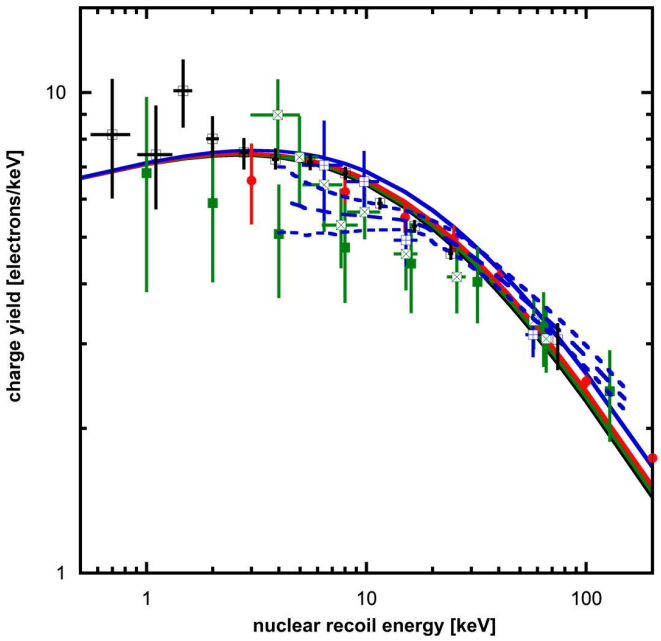

Figure 1.3.9: Absolute NR ionization yield in LXe. Data are as follows: blue and green hollow squares from neutron beam data from Yale at 4 kV/cm and 1 kV/cm, respectively [62]; dashed blue curves from MC matching from ZEPLIN-III [64] at 3,650 V/cm; solid green squares from XENON10 at 730 V/cm[66]; red markers from XENON100 at 530 V/cm [67]; black squares from LUX D-D neutron gun measurements in situ at 180 V/cm [23]. The NEST model is shown in black, green, red, and blue for 180, 310 (LZ baseline), 530, and 3,650 V/cm, respectively. The green curve is used for LZ sensitivity calculations.

the experimental data suggest a remarkably high yield even for 1-keV recoils, with several electrons being released per interaction. As with the scintillation yield, the electric field dependence is modest.

1.3.3.1 Low Energy and Low Mass Sensitivity

The high ionization yield allied to the ability to detect single electrons with high efficiency is a very attractive feature of this technology: Not only does it provide a low-threshold channel for light WIMP searches but, from a practical standpoint, it allows very high triggering efficiency (on S2) for the lowest-energy events, which are associated with very small S1 pulses.

Double-phase Xe detectors achieve the best NR energy threshold among the leading WIMP-search technologies, while maintaining discrimination and good vertex location. Of all such detectors operated so far, LUX can claim the lowest 50% NR threshold of approximately 4 keV. WIMP masses down to $\sim$10 GeV/c^2 are directly accessible to an instrument such as LZ operating in the "normal" TPC mode, requiring one S1 pulse and one S2 pulse. A low-energy ER interaction ($\approx$1.5 keV$_{ee}$) is shown in Figure 1.3.10 – 3-D position resolution and discrimination are fully effective even at these energies.

At the smallest NR energies ($\lesssim$4 keV$_{nr}$), it is clear that the S1 signal is often absent but S2 is still easily detectable, so that LZ can recover sensitivity in this regime by performing an "S2-only" analysis [68]. Discrimination based on S2/S1 ratio is not possible in this instance, but the detector retains the ability to reject edge events in (x, y). A more limited but still useful degree of z position reconstruction is possible based on the broadening of the S2 pulse due to longitudinal diffusion of electrons as they drift in the liquid. As a re-

sult, an S2-only search can still exploit the extremely radio-quiet inner region of the WIMP target, and place upper limits on the dark matter scattering cross section. Naturally, a thorough understanding of backgrounds is required for this type of analysis; several background mechanisms create single S2 electrons, while the two-electron random coincidence rate might still be significant. This technique is particularly applicable to particle masses lower than about 10 GeV/c^2.

One class of NR event that inevitably will be visible below the (3-phe) S1 threshold is due to coherent elastic scattering of ^{8}B solar neutrinos off Xe nuclei. The electron counting technique (S2-only) was in fact suggested a decade ago to allow a first observation of this process [69]. Due to energy resolution broadening of the scintillation signal, some events will register both S1 and S2—from this and other neutrino fluxes. Despite significant interest in this signal per se, coherent neutrino-nucleus scattering is also a fundamental background for dark matter searches, which is quantified in Chapter 2.2.1.2.

1.3.4 Electron/Nuclear Recoil Discrimination

Discrimination of ER/NR is key to the positive identification of a WIMP signal, both by directly reducing the effect of the dominant electronic backgrounds in the detector, and by confirming a NR origin. The physical basis for discrimination is the difference in the ratio of ionization electrons to scintillation photons that emerge from the interaction site and subsequently create the measured S2 and S1 signals, respectively. In a plot of the logarithm of S2/S1 as a function of S1, as in Figure 1.3.11, electron and nuclear recoils each form a distinct band, with NRs having a lower average charge/light ratio.

A figure of merit for discrimination is commonly the ER leakage past the median of the NR population (i.e., retaining a flat 50 % NR acceptance). Previous values are between 99.5 % in XENON10 [37] and 99.99 % in ZEPLIN-III [41]. We assume a baseline discrimination value of 99.5 %, a conservative assumption given the performance already obtained in LUX, as discussed below.

Electron/nuclear recoil discrimination is determined by the separation of the bands as well as their widths, and in particular the "low tail" in $\log_{10}$(S2/S1) of the ER band. Remarkably, the bands are mostly Gaussian when binned in slices of S1. Some skewness in the shape of the ER band has been observed in both the ZEPLIN-III and LUX experiments. In ZEPLIN-III, this skewness was observed using an external gamma-ray source whilst running at a high field [41]. Conversely, in LUX, the effect was seen when running an internal tritium calibration at a much lower electric field [58].

The physics determining both the position of the bands and their widths has been studied and we are increasingly able to model it successfully [71]. The overall separation of the bands is mostly due to NRs producing less initial ionization and more direct excitation (leading to scintillation) than do ERs. In turn, the band widths depend strongly on the physics of electron-ion recombination at the interaction site. A recombination episode generates an excited Xe atom that de-excites through scintillation (via the Xe_2^* state). Therefore, initial ionization is either measured as charge (via S2) or light (via S1), and event-by-event fluctuations in the amount of recombination are one of the primary sources of band broadening. These fluctuations increase with recoil energy over the range of interest.

At the lowest energies, however, the distributions "flare up" due to statistical fluctuations in the S1 signal. This broadening is therefore reduced in chambers with higher light yield, improving discrimination. In fact, ER rejection in this technology is better just above threshold (~5 keV to 15 keV), where WIMP-induced recoil rates are highest, than at intermediate energies (~15 keV to 40 keV), and then improves dramatically beyond ~40 keV. The excellent ER discrimination at low energies is due in part to a decrease of recombination fluctuations, but is also caused by the curvature of both bands at low energy, as shown in Figure 1.3.11: The bands are largely parallel to the direction of S1 fluctuations, sharply reducing their impact on discrimination.

In addition to light collection, the drift field is also expected to affect discrimination. Although largely determined by the amount of initial ionization, the positions of the band medians have a residual dependence

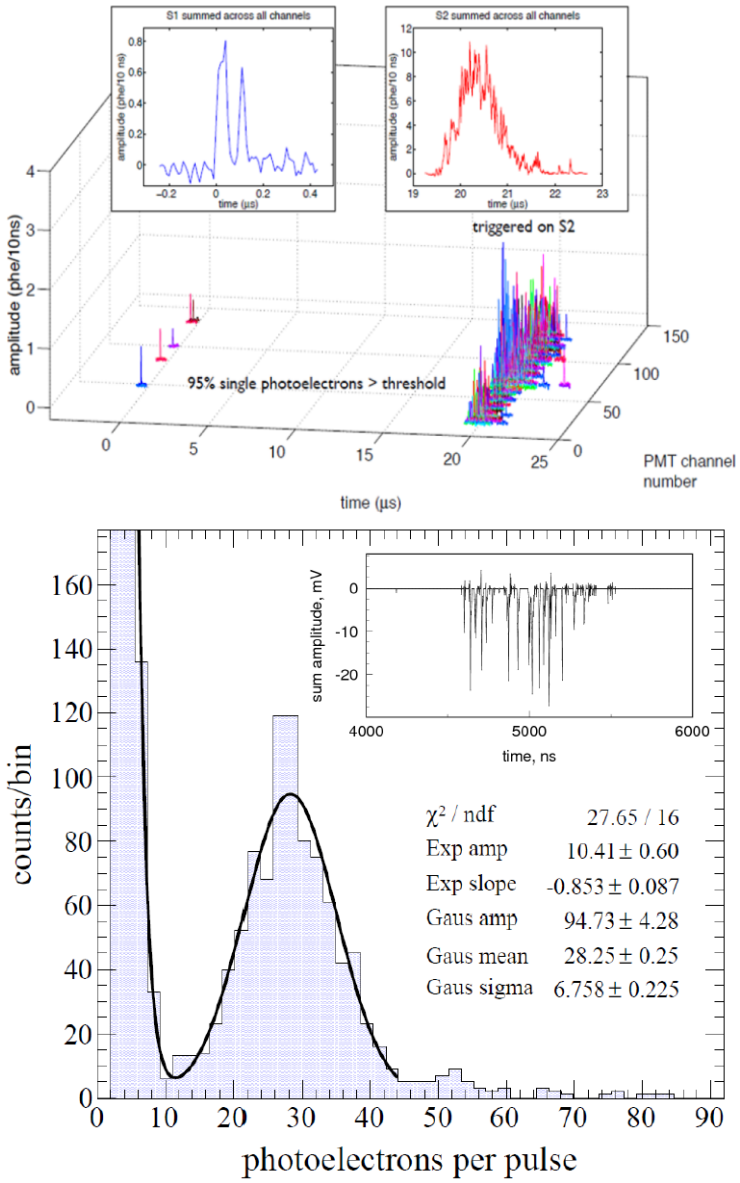

Figure 1.3.10: Low-energy performance of double-phase Xe detectors. Top: A 1.5 keV_{ee} electron interaction in LUX [70], showing a fivefold coincidence for S1 and the corresponding (much larger) S2 delayed by 20 µs. Bottom: Pulse size distribution of single electrons measured by electroluminescence in ZEPLIN-III, showing a mean of 28 photoelectrons per emitted electron (one such waveform is shown in inset) [44].

on the different amounts of field-dependent recombination for the two recoil species, and their separation increases at higher fields [71]. This may explain the world-best discrimination observed in ZEPLIN-III, which operated with close to 4 kV/cm drift field, and is an important driver of the LZ design. The band width should, in principle, also have some field dependence, though this has not been well measured. The model developed in [71] has been incorporated in the NEST Monte Carlo package [60, 65], which has informed the sensitivity projections for this report. However, caution must be exercised when comparing values from different experiments, since instrumental effects other than electric field and light yield can impact discrimination very severely. A case in point is the degraded discrimination measured in the second science run (SSR) of ZEPLIN-III [72] relative to the first science run (FSR) [41], benchmarked essentially in the same detector and with the same software, but following upgrade of the TPC with underperforming photomultipliers.

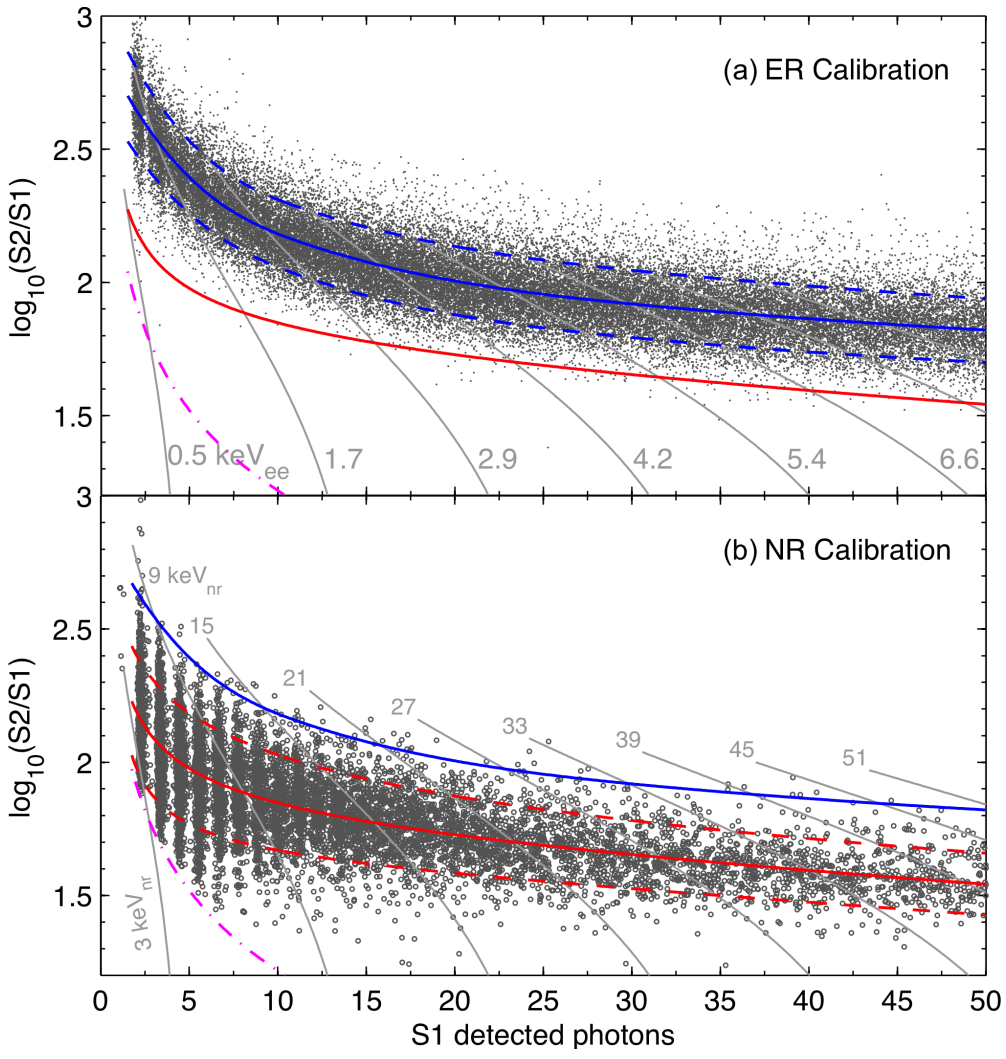

Figure 1.3.11: Discrimination parameter $\log_{10}$(S2/S1) as a function of S1 signal obtained with LUX calibration [58]. (a) ER band calibrated with beta decays from a dispersed ^{3}H source; the median is shown in blue, with 80 % population contours indicated by the dashed blue lines. (b) NR band populated by elastic neutron scattering from a D-D pulsed neutron source; the median (solid) and 80 % band width (dotted) are indicated in blue and red, respectively. The mostly vertical gray lines are contours of constant energy deposition. For more information, see Chapter 7.

The question of discrimination is of great importance in LZ, as its dominant background is ERs from ^{222}Rn and ^{220}Rn daughters as well as from solar neutrinos. To predict the LZ sensitivity, the electric field strength and the light-collection efficiency in the WIMP target are the main ingredients required. These are key performance parameters and we motivate their choice in two separate sections below; we also describe the steps we are taking to achieve the required performance. We use these parameters in conjunction with a full GEANT4 Monte Carlo simulation [73] based on the LUXSim package [74] and incorporating NEST.

The adopted values —a drift field of 310 V/cm and an S1 photon detection efficiency (PDE) of 7.5 % —motivate an average nominal discrimination of 99.5 % for a flat ER spectrum such as that from ^{222}Rn and ^{220}Rn as well as from pp neutrinos (an ER leakage past the NR median of 1:200). This is supported by both NEST-based simulations and by XENON10 [37], which achieved that level of discrimination at similar field and light collection as proposed here. PANDA-X recorded 99.7 % at 667 V/cm, for a PDE of 10.5 % [75]. Significantly, LUX initially reported 99.6 % discrimination at only 180 V/cm in Run 3 [30], increasing to 99.8 % in a subsequent reanalysis with improved algorithms [58]. Therefore, we are confident of reaching the 99.5 % value assumed in this report.

In fact, Figure 1.3.12 shows that the discrimination generally improves for smaller S1 signals, as measured in LUX. Further, the signal from a light WIMP is not distributed symmetrically around the NR median: Upward fluctuations in S1 that cause low-energy events to exceed a given analysis threshold also induce a distribution in $\log_{10}$(S2/S1) that is systematically lower than the NR median [76], as shown in Figure 2.2.1, Figure 12.3.1, and Figure 12.3.3. The acceptance of the ER rejection cut for light WIMPs is higher than the 50 % one might surmise from the median of the average NR distribution.

Phenomenon like those discussed in the previous paragraph, combined with the high-statistics calibrations recently completed by the LUX collaboration [45, 58], have convinced us to replace the simple 'cut-and-count' technique, and a simple leakage figure of merit, with the profile likelihood ratio (PLR) technique described in Section 12.3.1.

1.3.5 Outer Detector Systems

A WIMP scatter would deposit a few keV in the central volume of the LXe TPC, with no simultaneous energy deposit in surrounding materials. Neutrons caused by radioactivity, which can fake WIMP interactions when they scatter elastically, are likely to interact again either within the TPC or nearby, and so it is broadly desirable to replace as much of the neighboring material as possible with additional radiation detectors. It also helps to minimize intervening material between the active LXe in the TPC and any such ancillary detectors, namely by decreasing the thickness of the field-cage and of the cryostat vessels. Active material surrounding the central LXe volume also permits assessment of the local radioactivity environment, and thus to infer additional information on the backgrounds in the WIMP search region. A persuasive WIMP discovery will require excellent understanding of all background sources, which is best done through the characterization of those sources in situ.

The LZ apparatus will feature two distinct regions where active material surrounds the LZ TPC. The first is a "skin" of LXe, formed by liquid between the field cage and the inner vessel of the cryostat. The second is surrounding detectors of liquid scintillator (LS), which is doped with a small amount of gadolinium, to enhance its capability for neutron detection. We expect a threshold of 100 keV$_{ee}$ to 200 keV$_{ee}$ for both systems, with the gadolinium-doped LS detecting neutrons more effectively and the skin detector performing best for internal gamma rays.

1.3.5.1 Xenon Skin Veto

The side skin region consists of an unavoidable 4 cm to 8 cm of LXe between the outer boundary of the field cage and the inner boundary of the cryostat. An even thicker LXe region, known as the dome skin, exists

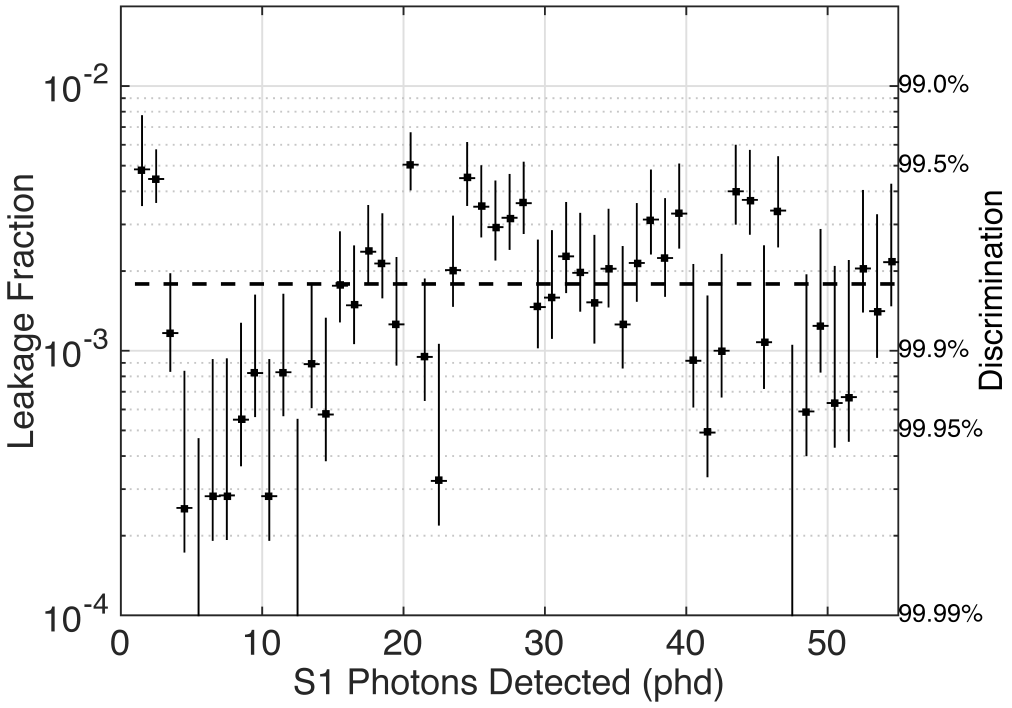

Figure 1.3.12: ER leakage fraction past the NR median line measured with tritium data in LUX. The dashed line indicates the average leakage of 0.002 (99.8 % discrimination) in the S1 range 2 phe to 50 phe. The general improvement of discrimination at low energies can be clearly seen, with the exception of the very lowest S1 data points where the ER band starts to flare up due to photoelectron statistics.

below the bottom PMT array. It is highly desirable to read out scintillation light generated in these regions for two main reasons:

1. They comprise anticoincidence detectors, where presence of a signal indicates that an interaction in the central LXe TPC is not from a WIMP.
2. They will also veto external LXe interactions where VUV photons could leak into the TPC and fake S1 light there.

Our approach is to maximize the optical isolation between inner and outer LXe volumes as far as practicable, and to instrument as much outer LXe as possible. Nevertheless, the sensitivity to deposited energy in the skin region will be far less than that of the central Xe TPC and, no ionization can be detected in the skin. Reasonable utility for the vetoing of gamma rays in the skin results when the threshold is a small fraction of the typical energy of an environmental gamma. To achieve this threshold, the side skin is equipped with 90 Hamamatsu R8520-406 PMT looking downwards and another 90 looking upwards to monitor the cylindrical shell between the sides of the TPC and the cryostat wall. The dome skin is viewed by 12 Hamamatsu R11410-22 PMT.

The PMT system achieves a threshold of about 100 $\mathrm{keV_{ee}}$, sufficient to detect Compton recoils from MeV gamma rays from radiogenic backgrounds. The skin detector will have low sensitivity for neutron detection via elastic scattering due to the mismatch in mass between neutrons and Xe nuclei, but inelastic neutron interactions can be detected in the skin, as can gamma rays produced by neutron capture. The LXe skin veto has some advantages over the outer detector for gamma detection because some gamma rays do not penetrate the various vessels all the way to the OD.

1.3.5.2 Scintillator Outer Detector

The goal of the outer detector is to surround the LZ cryostat with a near-hermetic gamma-ray and neutron anticoincidence system. LZ will employ linear alkyl benzene (LAB), an LS solvent developed by the reactor neutrino community in the past decade [77, 78]. Small quantities of a standard fluor and wavelength shifter will be added to the solvent to provide the scintillation signal. A PMT system located in the water space outside of the clear acrylic tanks containing the LS will view this scintillation light.

To enhance neutron detection, 0.1 % by weight of natural gadolinium will be dissolved in the LAB with a chelating agent to form Gd-loaded LS, or GdLS. Two isotopes of Gd, ^{155}Gd and ^{157}Gd, have neutron-capture cross sections that are 61 and 254 kb, respectively. Each of these isotopes constitutes about 15 % of natural Gd and, at 0.1 % concentration by weight, capture on Gd is about 1 order of magnitude more probable than is capture on hydrogen.

A neutron that can cause a Xe NR in the same energy range as the recoil from a WIMP will have an energy between about 0.5 and 5 MeV. The source of most of these neutrons will be from the (α, n) process from material around the edges of the Xe, and their energy spectrum will be toward the low end of this interval. A dangerous neutron will enter the LXe TPC and then scatter back out after one interaction. Many of those neutrons will traverse the intervening material and then thermalize and capture in the Gd in the GdLS. The length scale for thermalization and capture is a few centimeters and the typical capture time is ~30 µs, which is small compared with the 670 µs maximum drift time of the TPC.

After capture on Gd, a total energy of about 8 MeV is emitted as a burst of several gamma rays, which then interact in the LS (or the skin, or the TPC). This large energy release separates neutron captures from the γ rays from natural radioactivity, which die out above 3 MeV. The thickness of the GdLS layer is 61 cm, determined by detailed GEANT4-based simulations and mechanical consderations.

For a fraction of γ-rays that deposit energy in the central LXe TPC, the outer detector system also functions as a γ-ray veto, for those that propagate through the LXe skin and cryostat; these share the same detection requirements as the capture gammas. To achieve good efficiency as a γ-ray veto, we require a threshold to Compton electrons near 200 $\mathrm{keV_{ee}}$, and we set a threshold goal of 100 $\mathrm{keV_{ee}}$

In reactor neutrino experiments, typically a single acrylic cylinder contains the Gd-loaded scintillator. Transport logistics preclude this solution for LZ, and instead segmentation of the volume into nine smaller tanks that can be transported through the shafts and drifts that lead to the Davis Cavern is the adopted solution. To enhance light collection, the outer surface of the LZ cryostat will be affixed with a diffuse white reflective layer of Tyvek® to reflect light into the 8-inch Hamamatsu R5912 PMTs that will surround the tanks. The 600 µm multilayer Tyvek® we plan to use has a reflectivity in excess of 95 %.

The goal is a sufficient PMT collecting power to achieve 100 $\mathrm{keV_{ee}}$ threshold. Our preliminary studies indicate that, by covering the cryostat in Tyvek® and employing another reflective cylinder outside of the PMT system, the collecting power of 120 8-inch PMTs is sufficient to achieve the required threshold.

The GdLS tanks will be surrounded by ultrapure water, and the distance to the water-space PMT system that detects the LS scintillation light must be sufficient to attenuate gamma rays from PMT radioactivity (these are not low-background models). A distance of 80 cm from the scintillator tanks to the PMTs reduces the rate from this source to less than 5 Hz.

The tightest specifications on radioactive impurities in the GdLS arise from considerations of deadtime caused by the outer detector system. Our goal is a false veto probability that does not exceed 5 % over a 500 µs time window, which results in goals for radioactive impurities of <1.3 ppt U, <4.5 ppt Th, <0.8 ppt ^{40}K, and $<13 \times 10^{-18}$ g/g of ^{14}C. Our requirements on impurities are <10 ppt U, <20 ppt Th, <3 ppt ^{40}K, and $<15 \times 10^{-18}$ g/g of ^{14}C, which permit a 5 % inefficiency at 5 % false veto probability for a shorter 170 µs time window.

While the LAB itself generally exceeds the impurity goals, the additives must be purified somewhat more completely than has been achieved in the reactor neutrino experiments. The purity achieved by the Borexino

Collaboration greatly exceeds the LZ requirements for U / Th / K. Borexino demonstrated a ^{14}C impurity slightly better than that needed for LZ [79]. Should the ^{14}C level be higher than our goal or requirement, we are able to set a threshold of 200 keV$_{ee}$, above the endpoint of ^{14}C β decay.

Chapter 7 details the implementation and performance of the outer detector more fully.

1.4 Internal Calibration with Dispersed Sources

The physics of self-shielding allows LZ to achieve its unprecedented sensitivity by reducing the rate of γ-ray scatters in the energy range of interest to a level of secondary importance. This is the central feature of the LZ detector design. Conversely, the same effect presents a challenge for a calibration program based solely on external γ-sources such as ^{137}Cs, which range out in the first several centimeters.

LZ will use a suite of gaseous sources introduced into the xenon circulation path that will mix throughout the TPC active region and the xenon skin. In the active region we will rely primarily on the two sources that were developed and successfully used by LUX. ^{83m}Kr, a source of 9.4 keV$_{ee}$ and 32.1 keV$_{ee}$ conversion electrons, separated in time by an average of 154 ns, will be used to frequently calibrate spatial effects over the course of the run. However, owing to its complex decay structure and relatively high energy compared with the WIMP-search energy range, it is not suitable for calibrating the ER background.

The ^{83m}Kr has a 1.8 hour half-life and will decay away quickly enough that no removal is required. However, because of the slow mixing of the xenon in LZ, that isotope may not populate the active region uniformly. Therefore, LZ will also use ^{131m}Xe, which has a 164-keV x-ray and an 11-day half-life, to occasionally make a homogeneous distribution of events to uniformly calibrate position-dependent effects. Its higher energy is also well suited to calibrating the xenon skin at the expected threshold of about 100 keV$_{ee}$. For calibrating the ER background in the WIMP-search energy range, we will use tritium (^{3}H), a β^--emitter with a Q-value of 18.6 keV$_{ee}$, in the form of tritiated methane. As we demonstrated in LUX, this molecule can be effectively removed by the purification system without leaving residual activity and its energy is ideally suited for modeling the ER band down to threshold.

Further calibration of the skin will use higher-energy events from ^{220}Rn, a source of 6-MeV alpha particles. Unlike ^{222}Rn, this isotope has no long-lived progeny and presents no background contamination concerns. Another benefit of ^{220}Rn is that some of its progeny should live long enough to deposit on the detector walls and produce a useful calibration of the S2 response there, which as we have seen in LUX, is different than in the bulk.

1.5 Xenon Purity for Detector Performance

The fluid nature of LXe provides an opportunity to manipulate the purity of the LZ target material. The previous section describes how this allows internal calibration sources to be temporarily introduced into the LXe. This section considers how the purity can be maximized for low-background physics running. We consider two classes of impurities: the radioactive noble gases ^{85}Kr and ^{222}Rn– although the latter is addressed fully only in Chapter 9 – and electronegative contaminants such as oxygen and water.

Electronegative impurities are introduced during operations by the outgassing of detector materials, and they must be continuously suppressed to the level of ~0.1 ppb by the purification system to ensure good charge and photon transport. Previous detectors such as ZEPLIN-III achieved this through clean construction techniques with low-outgassing materials (i.e., no plastics), which allowed these systems to maintain purity without recirculation [80]. In larger detectors such as LUX, the need to utilize large volumes of PTFE (see Chapter 3 for detail) demands active recirculation in the gas phase. The efficient removal of electronegative contaminants is made possible by purification technology developed for the semiconductor industry. The

central elements of this technology are a heated zirconium getter for the removal of non-noble species, UHV-compatible plumbing and instrumentation, and a gas-circulation pump.

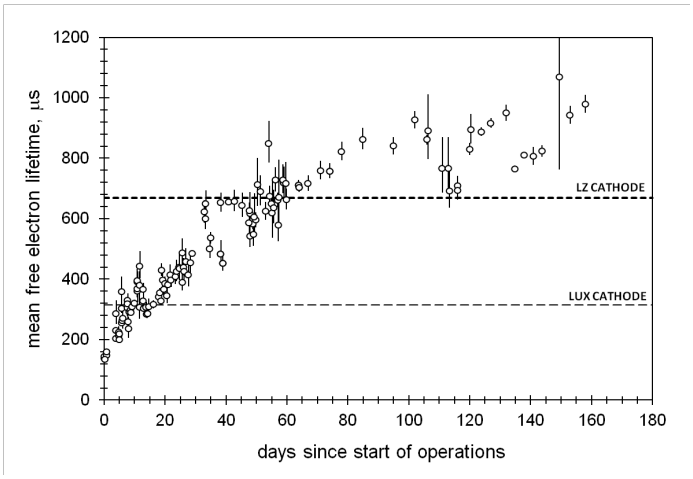

Figure 1.5.1: Evolution of the mean free electron lifetime in LUX during Run 3. The electronegative purity required to observe signals from the LZ cathode (∼670 µs for the 147-cm long TPC) has already been achieved in LUX.

Despite the availability of this technology, until recently the achievement of good electronegative purity in a LXe TPC was considered a significant technical challenge. What was lacking was an economical and sensitive monitoring technique to allow the purification technology to be fully exploited. While free electron lifetime monitors for LXe were developed over 20 years ago, these devices cannot identify individual impurity species, are insensitive to noble gas impurities, and provide little guidance on the origin of any impurities.

LZ scientists have developed a mass spectrometry method that allows most electronegative and noble gas impurities to be individually monitored in real time [52]. Most crucially, the method provided, for the first time, information on the impurity source. For example, the presence of an air leak introduces N_2, O_2, and Ar in a characteristic ratio, while a large excess of N_2 is a signature of a saturated purifier. Outgassing, on the other hand, leads to a uniform rate of increase of all common impurity species.

Experience with the mass spectrometry method, relevant to LZ, has been gained by applying it not only to LUX, but also to the EXO-200 $0\nu\beta\beta$-decay experiment [81]. Both experiments achieved their purity goals with relative ease due in part to the effectiveness of this program, and this valuable experience can be brought to bear on LZ. We have learned, for example, that vendor-supplied Xe is often relatively pure of electro-negatives; that zirconium getters are effective for Xe purification but that their performance degrades at higher gas flow rates; and that purifier performance improves at elevated temperature. This experience is of direct relevance for the design of the LZ purification system. In LUX, electron lifetimes of the order of 1 ms have been demonstrated, as shown in Figure 1.5.1, which is already sufficient to drift charge from interactions near the LZ cathode.

An additional benefit is that the method is sensitive not only to electronegatives but also to trace quantities of noble gas impurities, which is of critical importance for control of krypton. Krypton is a particularly dangerous impurity for LZ because of the presence of the beta emitter ^{85}Kr. This isotope, whose abundance at present is $\sim 2 \times 10^{-11}$ (^{85}Kr / $^{\mathrm{nat}}$Kr), presents the leading purification challenge for LZ because its noble nature makes it impervious to the zirconium getter technology. Vendor-supplied Xe typically contains about 100 ppb of $^{\mathrm{nat}}$Kr, which, if left untreated, would give rise to an ^{85}Kr β decay rate of 29 mBq/kg of Xe.

LZ will capitalize on the success of EXO-200 and LUX by integrating sensitive monitoring into its Xe handling program from the time of Xe procurement until the conclusion of the experiment. In addition, because the origin of impurities is now understood to be primarily due to outgassing, we have in place a comprehensive and extensive materials outgassing screening program.

While sensitive impurity monitoring will lay the groundwork for the LZ Xe purification program, the heart of the program to reduce long-lived noble-element radioisotopes will be the krypton removal program using

the chromatographic technique developed by LZ scientists now at SLAC [51]. This program was successfully applied to LUX and will be scaled up in mass-throughput by a factor of 20 for LZ. The krypton concentration goal is 0.015 ppt (g/g), a factor of 300 below the LUX goal but only a factor of 10 worse than the upper limit of 0.2 ppt (g/g) demonstrated so far with this method. At 0.2 ppt (g/g), the rate of beta decays from ^{85}Kr in the region of interest is comparable to the pp neutrinos. In parallel, the krypton detection limit of the mass spectrometry method has been improved to ∼0.015 ppt (g/g). The ultimate source of krypton impurities in LZ will be the outgassing of detector materials, which we can control through careful materials selection and through our outgassing plan.

Similarly, ^{222}Rn must be controlled by limiting the emanation sources within the detector and the gas system via a careful screening program. In fact, the need to limit radon and krypton in the LZ Xe is a driving consideration in the choice of key Xe system components such as the gas-recirculation pump. More generally, the materials-screening program is occurring hand-in-hand with the design efforts of all systems whose materials touch Xe, in order to ensure that systems meet both their technical and their background requirements on schedule.

1.6 Dominant Backgrounds

LZ has a clear background-control strategy with optimal exploitation of self-shielding to pursue an unprecedented science reach. These are the most salient features of this strategy: (1) underground operation within an instrumented water tank to mitigate cosmogenic backgrounds; (2) deployment of a target mass large enough to self-shield external radioactivity backgrounds, working in combination with outer, anticoincidence detectors; (3) construction from low-activity materials and purification of the target medium to render intrinsic backgrounds subdominant; and (4) rejection of the remaining ER backgrounds by S2/S1 discrimination.

The dominant fixed-contaminant radioactive backgrounds come from the Xe-space PMTs. This background is small when compared to that from radon. Our approach is to self-shield those sources over the first few centimeters of active liquid and thereby be sensitive to a population of ERs caused by elastic scattering of solar pp neutrinos – which can be further discriminated by their S2/S1 ratio. An irreducible but very small background of NRs will also arise from coherent neutrino-nucleus scattering. To achieve this we must reduce any intrinsic ER backgrounds contained within the Xe itself to a tolerable level, with ^{85}Kr, ^{39}Ar, and Rn progeny being a particular challenge. Electron recoils caused by the $2\nu\beta\beta$ decay of ^{136}Xe, now confirmed by the EXO-200 [82] and KamLAND-Zen [83] experiments, are subdominant below about 20 keV$_{ee}$. Cosmogenic (muon-induced) backgrounds are not significant during operation due to the tagging capability of the instrumented water tank and the scintillator veto, but cosmogenic activation of detector materials prior to deployment (including the Xe) must be addressed.

We describe briefly some of these background categories here (radioactivity external to the TPC, intrinsic contamination of the LXe, and cosmogenic backgrounds), as these are important LZ sensitivity drivers, but we offer a full discussion on their mitigation to Chapter 9. Neutrino backgrounds are explored further in Chapter 2. The solar pp neutrino scattering rate of 0.8×10^{-5} events/kg/d/keV (ee) is the benchmark against which other rates are assessed.

1.6.1 Backgrounds from Material Radioactivity

Radioactivity backgrounds have limited nearly all dark matter experiments so far and, in spite of the power of self-shielding, we are not complacent in addressing them in LZ. They impact the thickness of the sacrificial layer of LXe that shields the fiducial mass, and they may cause rare-event topologies that may be of consequence (from random coincidences, atypical surface interactions, or Cherenkov emission in PMT glasses, for example). It is important, therefore, to minimize the rate of α, β, and γ activity around the active

volume, as well as neutron production from spontaneous fission of ^{238}U and from (α,n) reactions. In addition, the rate and spatial distribution of such backgrounds must be well characterized to build an accurate background model for the experiment. The LZ background model is derived from a high-fidelity simulation of the experiment in the LUXSim framework, which was successfully used for the LUX background model [84].

All materials to be used in LZ will be subject to stringent constraints as part of the comprehensive screening campaign described in Chapter 9, with 10 % of the solar pp neutrino scattering rate and a maximum of ~0.2 NRs at 50 % signal acceptance being the target for the total contribution from material radioactivity within the fiducial volume. The dominant rates come from the various PMT systems and the LZ cryostat, based on the large masses and close proximity to the active region of the detector. Table 1.6.1 summarizes the count rates from neutron and γ-ray emission expected from detector materials and other backgrounds, which are discussed in greater detail in Chapter 9. Here and hereafter count rates are given for an indicative 5.6-tonne fiducial mass, considering only single scatter events with no accompanying signal in either the LXe skin or the Outer detector veto systems. The region of interest for WIMP searches is defined as 1) the number of detected photons in the S1 signal to be greater than 0 and less than 20, 2) 3-fold coincidence in S1 between PMTs in the target volume, 3) the number of detected photons in the S2 signal is greater than 350. This region of interest approximately corresponds to energy deposits of 6 keV to 30 keV for nuclear recoils and 1.5 keV to 6.5 keV for electron recoils. The range of energy deposits is sometimes used to reference the region of interest throughout the text. A full description of the analysis cuts is given in Chapter 12.

Table 1.6.1: Summary of backgrounds in LZ, showing the number of counts expected in 1,000 live days in an indicative 5.6-tonne fiducial mass in the region of interest with all cuts applied. A comprehensive set of numbers can be found in Table 9.2.7.

Item	ER cts	NR cts
Detector Componenents	6.2	0.07
Dispersed radionuclides (Rn, Kr, Ar)	911	-
Laboratory and cosmogenic	4.3	0.06
Fixed surface contamination	0.19	0.37
^{136}Xe $2\nu\beta\beta$	67	-
Neutrinos (ν-e, ν-A)	255	0.72
Total	1244	1.22
Total (with 99.5% ER discrimination, 50% NR efficiency)	6.22	0.61
Total ER+NR background events	6.83	

The PMTs chosen for the LZ TPC are Hamamatsu R11410s, which have achieved very low radioactivity values; LZ scientists have been involved in a long campaign to establish their performance for dark matter experiments, working actively with the manufacturer to enable this [48]. The PTFE required to fabricate the TPC field cage, skin reflectors, and other internal components may also be an important source of neutron emission from the bulk material. We use upper limits on the contamination measured by EXO-200 in calculating its impact [85]. The cryostat is another dominant component, mostly owing to its large mass. For the

titanium baseline design (2,140 kg), the total neutron emission rate is estimated at 0.6 n/day based on recent titanium samples procured for LZ. As a result of a 2-year material search campaign, we were able to find titanium with U/Th contamination, which is a factor of 2 lower than that used in LUX [49] as explained in Section 5.1.

1.6.2 Surface Plating of Radon Progeny

The noble gas radon consists solely of radioactive isotopes, of which four are found in nature: ^{222}Rn and ^{218}Rn produced in the ^{238}U decay chain, ^{220}Rn from the ^{232}Th decay chain, and ^{219}Rn from the ^{227}Ac series. As a result of its chemical inertness, radon exhibits long diffusion lengths in solids. ^{222}Rn is the most stable isotope ($T_{1/2}$ = 3.82 days), and is present in air at levels of about ten to hundreds of Bq/m^3. Charged radon progeny – especially metallic species such as ^{218}Po – plate out onto macroscopic surfaces that are exposed to radon-laden air. A fraction will deposit and even implant into material surfaces during detector construction or installation [86].

Backgrounds from surface beta and gamma radioactivity, as well as recoiling nuclei (e.g., ^{206}Pb from the alpha decay of ^{210}Po), are largely mitigated by short half-lives and the self-shielding of LXe. However, α-particles released in the decay chain, particularly from ^{210}Po – a granddaughter of the long-lived ^{210}Pb ($T_{1/2}$ = 22.3 years) – result in neutron emission following (α, n) reactions. This is problematic for TPC materials with large (α, n) yields such as PTFE ($\sim 10^{-5}$ n/α, due to the presence of fluorine). Additionally, because PTFE is produced in granular form before being sintered in molds, plate-out poses further risk because surface contamination of the granular form becomes bulk contamination when the granules are poured into molds.

A second concern relates to our ability to correctly reconstruct events at the TPC inner walls, since the imperfect reconstruction of these events leads to a background population leaking radially toward the fiducial volume [30, 35]. This concern drives the design of the top PMT array and places tight requirements on the plate-out of radon progeny on the TPC walls (see Section 3.4).

Controls to mitigate background from radon plate-out will include limiting the exposure of detector parts to radon-rich air; monitoring from point of production through transport and storage in Rn-proof materials; and employing surface cleaning techniques, such that neutron emission is negligible relative to material radioactivity from bulk uranium and thorium contamination.

1.6.3 Intrinsic Backgrounds

We are confident that our requirements for intrinsic radioactive contamination from ^{85}Kr and ^{222}Rn can be met with the Xe-purification techniques described in Chapter 6, coupled with the radon emanation screening of Xe-wetted materials described in Chapter 9. We note that most of these backgrounds can be estimated with low systematic uncertainty. In addition to direct sampling, the ^{85}Kr β- decay spectrum is well understood and the decay rate can be measured during operation with delayed $\beta-\gamma$ coincidences.

Other delayed coincidence techniques as well as α spectroscopy allow precise estimation of radon-induced backgrounds. In fact, it is possible to follow dynamically the spatial distribution of these decays throughout the detector, which was done very successfully in LUX [87]. The two main concerns in this instance are a "weak" naked β-decay from ^{214}Pb in the bulk of the TPC (E_{max} = 1,019 keV, BR = 9.2 %), and the possibility of γ-ray escape for peripheral events from the dominant ^{214}Pb decay modes.

Our goal is to control each of these two backgrounds to <10 % of the solar pp neutrino rate, limiting the ^{222}Rn activity to 0.67 mBq and the krypton concentration to 0.02 ppt (g/g). In a more conservative scenario, as requirements we allow the sum of these two components to be 3 times the ER background from pp neutrinos.

Trace quantities of argon are also a concern due to β-emitting ^{39}Ar, with a 269-year half-life and 565 keV endpoint energy. This background is constrained to be less than 10 % of ^{85}Kr, resulting in a specification of 4.5×10^{-10} (g/g) or 2.6 µBq. The Kr-removal system, which also removes Ar, should easily achieve this.

1.6.4 Cosmogenic Backgrounds

A rock overburden of 4,300 m w. e. above the Davis Cavern at SURF reduces the muon flux by about a factor of 3×10^6 relative to the surface [88, 89]. Muons crossing the water tank and/or liquid scintillator are readily detected via Cherenkov emission in water and/or scintillations, and any coincident energy deposition in LZ is similarly easily identified. However, neutron production in muon-induced electromagnetic and hadronic showers, in particular in high-Z materials, may generate background events [90, 91]. The total muon-induced neutron flux at SURF from the surrounding rock is calculated to be about 0.5×10^{-9} n/cm^2/s, with approximately half of this flux coming from neutrons above 10 MeV, and some 10 % from energies above 100 MeV [92, 93].

Muon-induced neutrons generated in the water shield and liquid scintillator produce a similarly low rate, despite the several hundred tonnes of target mass, due to the low atomic number of water and scintillator and consequent low neutron yield ($\sim 2.5 \times 10^{-4}$ n/muon/(g/cm^2)), translating to a production rate of order of 10^{-9} n/kg/s).

Cosmogenic activation – radioisotopes production within materials, largely through spallation reactions of fast nucleons from cosmic rays while on the Earths surface – can present electromagnetic background in LZ. ^{46}Sc produced in the titanium cryostat decays through emission of 889 keV and 1,120 keV γ-rays (with $T_{1/2}$ = 84 days). Cosmogenic ^{60}Co ($T_{1/2}$ = 5.3 years) in copper components will produce gamma rays of 1,173 keV and 1,332 keV.

Activation of the Xe itself during storage or transport generates several radionuclides, some of which are important, especially in the first few months of operation. Tritium ($T_{1/2}$ = 12.3 years and production rate of ~15 /kg/day at the Earths surface [94]) was previously a concern; however, this is effectively removed through purification during operation. Production of Xe radioisotopes, such as ^{127}Xe ($T_{1/2}$ = 36.4 days), ^{129m}Xe ($T_{1/2}$ = 8.9 days), and ^{131m}Xe ($T_{1/2}$ = 11.9 days), are more problematic, as they cannot be mitigated through self-shielding or purification. In particular, atomic de-excitation of the 2s and 3s shells in ^{127}Xe generates 5.2 and ≤1.2 keV energy deposits, respectively, which are an important background in the WIMP search energy region for certain event topologies [30]. These backgrounds soon reach negligible levels once Xe is moved underground.

1.6.5 Fiducialization

The backgrounds from nearby materials cluster near the edges of the LZ central TPC, and they fall off according to an exponential distributions described in Fig. 1.3.5. The rapid fall off of backgrounds from material radioactivity suggests the definition of a fiducial volume, which is an inner region that is relatively free of background.

The fiducial volume is a simplification that allows intuitive understanding of the LZ background from nearby materials. Eventually, LZ will abandon the concept of a fiducial volume in favor of a PLR maximum likelihood fit which describes the spatial distributions of the various background components, like the LUX collaboration has recently done [23].

We define an LZ fiducial volume that starts 1.5 cm above the cathode at the bottom of the TPC, 4 cm inside of the reflective walls that surround the TPC, and 13.5 cm down from the gate grid at the top of the TPC. This fiducial volume encloses 5.6 tonnes of LXe, and the event numbers tabulated in Table 1.6.1 occur inside this fiducial volume in a 1,000 live day run.

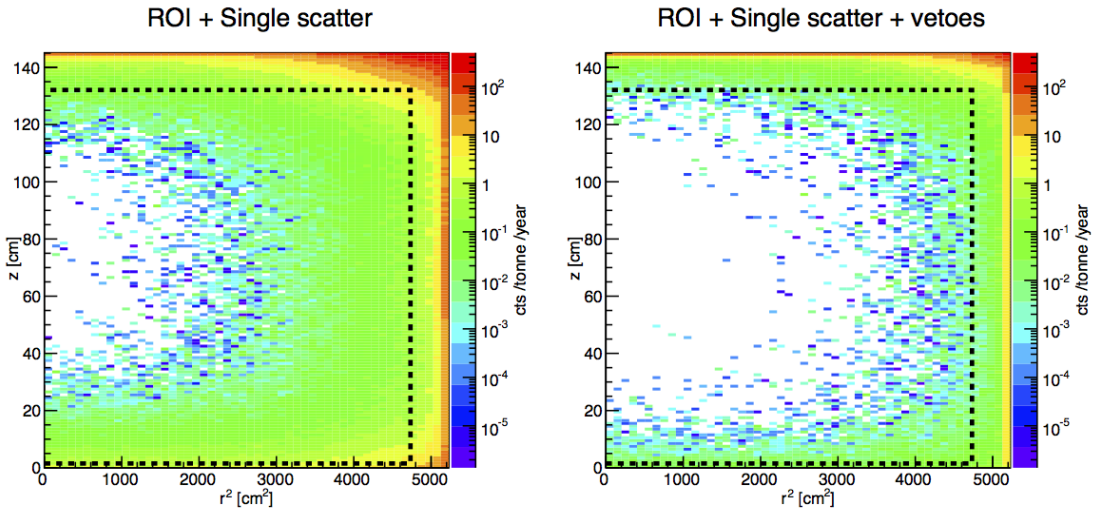

Figure 1.6.1: Total NR background plus ER leakage from material radioactivity for sources external to the LXe in the TPC, counted over a 6 keV to 30 keV acceptance region; a discrimination efficiency of 99.5 % is applied to ERs from beta decays and gamma rays. Left: Single scatters only, no vetoing by the anti-coincidence systems. Right: Adding the combination of both the skin veto and the outer detector. The dashed line shows the boundary of the 5.6 tonnes fiducial mass.

Two main factors determine how far the fiducial boundary should lie from the lateral TPC walls. The prime consideration is to ensure a sufficiently thick layer of LXe to self-shield against the external radioactivity backgrounds. This is related to the mean attenuation length for those particles: Figure 1.3.5 confirmed that ~2 cm of liquid decreases the γ-ray background tenfold, and as much as ~6 cm is needed to mitigate neutrons by the same factor. However, the outer detector is very efficient for neutron tagging, which brings these two requirements closer together.

Secondly, it is essential that the reconstructed (x,y) positions of low-energy interactions occurring near the TPC walls do not "leak" into the fiducial volume. As mentioned above (and discussed in Chapter 3) interactions from radon progeny plating the lateral PTFE are of particular concern: These can generate events with very small S2 signals due to trapping of charge drifting too close to the PTFE. If allied with poor position resolution, this can constitute a very challenging background [35]. In the vertical direction, only the former consideration arises. We point out that the reverse field region below the cathode will provide much of the required self-shielding (>14 cm), whereas at the top, the small thickness of liquid above the gate (0.5 cm) will have a limited impact.

Figure 1.6.1 shows the simulated background rate from material radioactivity in the WIMP region of interest (6 keV to 30 keV) as a function of radius squared and height above the cathode grid. Nuclear and electron recoil backgrounds were combined, with 50 % acceptance applied to the former and 99.5 % discrimination applied to the latter. The neutrino and dispersed background contributions listed in Table 1.6.1 are omitted from Figure 1.6.1 because they populate the figures uniformly.

The left panel of Figure 1.6.1 shows the rate of material backgrounds when neither of the outer detector systems, the LXe skin nor the outer detector, is utilized. The background-free region in the central TPC is small, and comprises about one-half of the 7 tonnes of active liquid xenon. The right panel shows the background rates after the application of the two outer detector systems, which enlarge considerably the background-free region. The event totals in Table 1.6.1 are computed from the events inside the fiducial volume enclosing 5.6 tonnes delineated by the dashed line in Fig. 1.6.1.

1.7 Bibliography

[1] D. N. Spergel *et al.* (WMAP), Astrophys. J. Suppl. **170**, 377 (2007), arXiv:astro-ph/0603449 [astro-ph].

[2] W. J. Percival *et al.*, Astrophys. J. **657**, 645 (2007), arXiv:astro-ph/0608636 [astro-ph].

[3] E. Komatsu *et al.* (WMAP), Astrophys. J. Suppl. **192**, 18 (2011), arXiv:1001.4538 [astro-ph].

[4] P. A. R. Ade *et al.* (Planck), Astron. Astrophys. **571**, A16 (2014), arXiv:1303.5076 [astro-ph].

[5] P. A. R. Ade *et al.* (Planck), Astron. Astrophys. **594**, A13 (2016), arXiv:1502.01589 [astro-ph].

[6] C. S. Frenk and S. D. M. White, Ann. Phys. (Berlin) **524**, 507 (2012), arXiv:1210.0544 [astro-ph].

[7] F. Governato, A. Zolotov, A. Pontzen, C. Christensen, S. H. Oh, A. M. Brooks, T. Quinn, S. Shen, and J. Wadsley, Mon. Not. R. Astron. Soc. **422**, 1231 (2012), arXiv:1202.0554 [astro-ph].

[8] A. Kusenko and L. J. Rosenberg, in *Planning the Future of U.S. Particle Physics, The Snowmass 2013 Proceedings*, edited by N. A. Graf, M. E. Peskin, and J. L. Rosner (2013); Working Group Report: *Non-WIMP Dark Matter*, arXiv:1310.8642 [hep-ph].

[9] B. W. Lee and S. Weinberg, Phys. Rev. Lett. **39**, 165 (1977).

[10] M. Cahill-Rowley, R. Cotta, A. Drlica-Wagner, S. Funk, J. Hewett, A. Ismail, T. Rizzo, and M. Wood, Phys. Rev. **D91**, 055011 (2015), arXiv:1405.6716 [hep-ph].

[11] G. Aad *et al.* (ATLAS), Phys. Lett. **B716**, 1 (2012), arXiv:1207.7214 [hep-ex].

[12] S. Chatrchyan *et al.* (CMS), Phys. Lett. **B716**, 30 (2012), arXiv:1207.7235 [hep-ex].

[13] D. Clowe, M. Bradac, A. H. Gonzalez, M. Markevitch, S. W. Randall, C. Jones, and D. Zaritsky, Astrophys. J. **648**, L109 (2006), arXiv:astro-ph/0608407 [astro-ph].

[14] A. Djouadi *et al.* (MSSM Working Group), in *GDR (Groupement de Recherche) - Supersymétrie Montpellier, France, April 15-17, 1998* (1998) arXiv:hep-ph/9901246 [hep-ph].

[15] C. F. Berger, J. S. Gainer, J. L. Hewett, and T. G. Rizzo, J. High Energy Phys. **2009**, 023 (2009), arXiv:0812.0980 [hep-ph].

[16] B. S. Acharya *et al.* (CTA), Astropart. Phys. **43**, 3 (2013).

[17] Y. Sofue, Publ. Astron. Soc. Jap. **64**, 75 (2012), arXiv:1110.4431 [astro-ph].

[18] J. Bovy and S. Tremaine, Astrophys. J. **756**, 89 (2012), arXiv:1205.4033 [astro-ph].

[19] R. Catena and P. Ullio, J. Cosmol. Astropart. Phys. **2010**, 004 (2010), arXiv:0907.0018 [astro-ph].

[20] K. Freese, J. A. Frieman, and A. Gould, Phys. Rev. **D37**, 3388 (1988).

[21] C. Savage, K. Freese, and P. Gondolo, Phys. Rev. **D74**, 043531 (2006), arXiv:astro-ph/0607121 [astro-ph].

[22] R. Agnese *et al.* (SuperCDMS), "WIMP-Search Results from the Second CDMSlite Run," (2015), submitted to Phys. Rev. Lett., arXiv:1509.02448 [astro-ph].

[23] D. S. Akerib *et al.* (LUX), Phys. Rev. Lett. **116**, 161301 (2016), arXiv:1512.03506 [astro-ph].

[24] P. Cushman *et al.*, in *Planning the Future of U.S. Particle Physics, The Snowmass 2013 Proceedings*, edited by N. A. Graf, M. E. Peskin, and J. L. Rosner (2013); Working Group Report:*WIMP Dark Matter Direct Detection*, arXiv:1310.8327 [hep-ex].

[25] K. Griest and M. Kamionkowski, Phys. Rev. Lett. **64**, 615 (1990).

[26] D. S. Akerib *et al.* (LUX), Phys. Rev. Lett. **118**, 021303 (2017), arXiv:1608.07648 [astro-ph.CO].

[27] P. Belli, R. Bernabei, S. D'Angelo, A. Incicchitti, and D. Prosperi, Nuovo Cim. **A103**, 767 (1990).

[28] G. J. Davies, W. G. Jones, J. D. Davies, J. D. Lewin, and P. F. Smith, Phys. Lett. **B320**, 395 (1994).

[29] P. Benetti *et al.*, Nucl. Instrum. Meth **A327**, 203 (1993).

[30] D. S. Akerib *et al.* (LUX), Phys. Rev. Lett. **112**, 091303 (2014), arXiv:1310.8214 [astro-ph].

[31] R. Agnese *et al.* (SuperCDMS), Phys. Rev. **D92**, 072003 (2015), arXiv:1504.05871 [hep-ex].

[32] R. Agnese *et al.* (SuperCDMS), Phys. Rev. Lett. **112**, 241302 (2014), arXiv:1402.7137 [hep-ex].

[33] P. Agnes *et al.* (DarkSide), Phys. Rev. **D93**, 081101 (2016), arXiv:1510.00702 [astro-ph].

[34] G. J. Alner *et al.* (ZEPLIN-I), Astropart. Phys. **23**, 444 (2005).

[35] G. J. Alner *et al.* (ZEPLIN-II), Astropart. Phys. **28**, 287 (2007), arXiv:astro-ph/0701858 [astro-ph].

[36] D. Yu. Akimov *et al.* (ZEPLIN-III), Astropart. Phys. **27**, 46 (2007), arXiv:astro-ph/0605500 [astro-ph].

[37] E. Aprile *et al.* (XENON10), Astropart. Phys. **34**, 679 (2011), arXiv:1001.2834 [astro-ph].

[38] V. Chepel and H. Araújo, J. Instrum. **8**, R04001 (2013), arXiv:1207.2292 [physics.ins-det].

[39] E. Aprile and T. Doke, Rev. Mod. Phys. **82**, 2053 (2010), arXiv:0910.4956 [physics.ins-det].

[40] V. N. Solovov *et al.* (ZEPLIN-III), IEEE Trans. Nucl. Sci. **59**, 3286 (2012), arXiv:1112.1481 [physics.ins-det].

[41] V. N. Lebedenko *et al.* (ZEPLIN-III), Phys. Rev. **D80**, 052010 (2009), arXiv:0812.1150 [astro-ph].

[42] B. Edwards *et al.* (ZEPLIN-II), Astropart. Phys. **30**, 54 (2008), arXiv:0708.0768 [physics.ins-det].

[43] P. F. Sorensen, *A Position-Sensitive Liquid Xenon Time-Projection Chamber for Direct Detection of Dark Matter: The XENON10 Experiment*, Ph.D. thesis, Brown U., Phys. Dept. (2008).

[44] E. Santos *et al.* (ZEPLIN-III), J. High Energy Phys. (Online) **2011**, 115 (2011), arXiv:1110.3056 [physics.ins-det].

[45] D. S. Akerib *et al.* (LUX), "Low-energy (0.7-74 keV) nuclear recoil calibration of the LUX dark matter experiment using D-D neutron scattering kinematics," (2016), submitted to Phys. Rev. **C**, arXiv:1608.05381 [physics.ins-det].

[46] A. Benoit *et al.* (EDELWEISS), Phys. Lett. **B513**, 15 (2001), arXiv:astro-ph/0106094 [astro-ph].

[47] D. Abrams *et al.* (CDMS), Phys. Rev. **D66**, 122003 (2002), arXiv:astro-ph/0203500 [astro-ph].

[48] D. S. Akerib *et al.* (LUX), Nucl. Instrum. Meth. **A703**, 1 (2013), arXiv:1205.2272 [physics.ins-det].

[49] D. S. Akerib *et al.* (LUX), "Radio-assay of Titanium samples for the LUX Experiment," (2011), (unpublished), arXiv:1112.1376 [physics.ins-det].

[50] D. S. Akerib *et al.* (LZ), Submitted to: Astropart. Phys. (2017), arXiv:1702.02646 [physics.ins-det].

[51] A. I. Bolozdynya, P. P. Brusov, T. Shutt, C. E. Dahl, and J. Kwong, in *Proceedings of the 11th Symposium on Radiation Measurements and Applications Ann Arbor, MI, USA 2326 May 2006*, Nucl. Instrum. Meth., Vol. **A579** (2007) pp. 50–53, *A chromatographic system for removal of radioactive ^{85}Kr from xenon*.

[52] D. S. Leonard, A. Dobi, C. Hall, L. Kaufman, T. Langford, S. Slutsky, and Y.-R. Yen, Nucl. Instrum. Meth. **A621**, 678 (2010), arXiv:1002.2742 [physics.ins-det].

[53] M. B. Chadwick *et al.*, Nucl. Data Sheets **112**, 2887 (2011), special issue on ENDF/B-VII.1 library.

[54] M. J. Berger *et al.*, XCOM: Photon Cross Section Database (version 1.5) (2010), National Institute of Standards and Technology, 100 Bureau Drive, Stop 1070, Gaithersburg, MD 20899-1070.

[55] E. Aprile *et al.* (XENON100), Phys. Rev. Lett. **109**, 181301 (2012), arXiv:1207.5988 [astro-ph].

[56] E. Aprile *et al.*, Phys. Rev. **D86**, 112004 (2012), arXiv:1209.3658 [astro-ph].

[57] L. Baudis, H. Dujmovic, C. Geis, A. James, A. Kish, A. Manalaysay, T. M. Undagoitia, and M. Schumann, Phys. Rev. **D87**, 115015 (2013), arXiv:1303.6891 [astro-ph].

[58] D. S. Akerib *et al.* (LUX), Phys. Rev. **D93**, 072009 (2016), arXiv:1512.03133 [physics.ins-det].

[59] M. Szydagis, N. Barry, K. Kazkaz, J. Mock, D. Stolp, M. Sweany, M. Tripathi, S. Uvarov, N. Walsh, and M. Woods (NEST), J. Instrum. **6**, P10002 (2011), arXiv:1106.1613 [physics.ins-det].

[60] M. Szydagis, A. Fyhrie, D. Thorngren, and M. Tripathi (NEST), *Proceedings, LIght Detection In Noble Elements (LIDINE2013)*, J. Instrum. **8**, C10003 (2013), arXiv:1307.6601 [physics.ins-det].

[61] B. A. Dolgoshein, V. A. Lebedenko, and B. U. Rodionov, JETP Lett. **11**, 351 (1970).

[62] A. Manzur, A. Curioni, L. Kastens, D. N. McKinsey, K. Ni, and T. Wongjirad, Phys. Rev. **C81**, 025808 (2010), arXiv:0909.1063 [physics.ins-det].

[63] G. Plante, E. Aprile, R. Budnik, B. Choi, K. L. Giboni, L. W. Goetzke, R. F. Lang, K. E. Lim, and A. J. Melgarejo Fernandez, Phys. Rev. **C84**, 045805 (2011), arXiv:1104.2587 [nucl-ex].

[64] M. Horn *et al.* (ZEPLIN-III), Phys. Lett. **B705**, 471 (2011), arXiv:1106.0694 [physics.ins-det].

[65] B. Lenardo, K. Kazkaz, A. Manalaysay, J. Mock, M. Szydagis, and M. Tripathi (NEST), IEEE Trans. Nucl. Sci. **62**, 3387 (2015), arXiv:1412.4417 [astro-ph.IM].

[66] P. Sorensen *et al.*, in *Proceedings, 8th International Workshop on The Identification of Dark Matter (IDM 2010)*, Proc. of Science, Vol. **IDM2010** (2011) p. 017, *Lowering the low-energy threshold of xenon detectors*, arXiv:1011.6439 [astro-ph].

[67] E. Aprile *et al.* (XENON100), Phys. Rev. **D88**, 012006 (2013), arXiv:1304.1427 [astro-ph].

[68] J. Angle *et al.* (XENON10), Phys. Rev. Lett. **107**, 051301 (2011), [Erratum: Phys. Rev. Lett. 110, 249901 (2013)], arXiv:1104.3088 [astro-ph].

[69] C. Hagmann and A. Bernstein, in *Proceedings, 2003 IEEE Nuclear Science Symposium, Room-Temperature Semiconductor Detector Workshop, and Symposium on Nuclear Power Systems (2003 NSS/RTSD/SNPS)*, IEEE Trans. Nucl. Sci., Vol. **51** (2004) pp. 2151–2155, *Two-phase emission detector for measuring coherent neutrino-nucleus scattering*, arXiv:nucl-ex/0411004 [nucl-ex].

[70] D. S. Akerib *et al.* (LUX), Astropart. Phys. **45**, 34 (2013), arXiv:1210.4569 [astro-ph].

[71] C. E. Dahl, *The physics of background discrimination in liquid xenon, and first results from Xenon10 in the hunt for WIMP dark matter*, Ph.D. thesis, Princeton U. (2009).

[72] D. Yu. Akimov *et al.* (ZEPLIN-III), Phys. Lett. **B709**, 14 (2012), arXiv:1110.4769 [astro-ph].

[73] S. Agostinelli *et al.* (GEANT4), Nucl. Instrum. Meth. **A506**, 250 (2003).

[74] D. S. Akerib *et al.* (LUX), Nucl. Instrum. Meth. **A675**, 63 (2012), arXiv:1111.2074 [physics.data-an].

[75] M. Xiao *et al.* (PandaX), Sci. China Phys. Mech. Astron. **57**, 2024 (2014), arXiv:1408.5114 [hep-ex].

[76] P. Sorensen, Phys. Rev. **D86**, 101301 (2012), arXiv:1208.5046 [astro-ph].

[77] X. Guo *et al.* (Daya Bay), "A Precision measurement of the neutrino mixing angle θ_{13} using reactor antineutrinos at Daya-Bay," (2007), proposal, arXiv:hep-ex/0701029 [hep-ex].

[78] F. P. An *et al.* (Daya Bay), Nucl. Instrum. Meth. **A685**, 78 (2012), arXiv:1202.6181 [physics.ins-det].

[79] G. Alimonti *et al.* (Borexino), Nucl. Instrum. Meth. **A600**, 568 (2009), arXiv:0806.2400 [physics.ins-det].

[80] P. Majewski *et al.* (ZEPLIN-III), in *Position sensitive detectors. Proceedings, 9th International Conference, PSD9, Aberystwyth, UK, September 12-16, 2011*, J. Instrum. **7**, C03044 (2012), arXiv:1112.0080 [physics.ins-det].

[81] A. Dobi *et al.*, Nucl. Instrum. Meth. **A675**, 40 (2012), arXiv:1109.1046 [physics.ins-det].

[82] N. Ackerman *et al.* (EXO-200), Phys. Rev. Lett. **107**, 212501 (2011), arXiv:1108.4193 [nucl-ex].

[83] A. Gando *et al.* (KamLAND-Zen), Phys. Rev. **C85**, 045504 (2012), arXiv:1201.4664 [hep-ex].

[84] D. S. Akerib *et al.* (LUX), Astropart. Phys. **62**, 33 (2015), arXiv:1403.1299 [astro-ph].

[85] D. S. Leonard *et al.*, Nucl. Instrum. Meth. **A591**, 490 (2008), arXiv:0709.4524 [physics.ins-det].

[86] V. E. Guiseppe, S. R. Elliott, A. Hime, K. Rielage, and S. Westerdale, in *Topical Workshop on Low Radioactivity Techniques: LRT-2010*, AIP Conf. Proc., Vol. **1338**, edited by R. Ford (2011) pp. 95–100, *A Radon Progeny Deposition Model*, Conference Presentation, arXiv:1101.0126 [nucl-ex].

[87] A. W. Bradley, *LUX Thermosyphon Cryogenics and Radon-Related Backgrounds for the First WIMP Result*, Ph.D. thesis, Case Western Reserve U. (2014).

[88] D.-M. Mei, C. Zhang, K. Thomas, and F. Gray, Astropart. Phys. **34**, 33 (2010), arXiv:0912.0211 [nucl-ex].

[89] V. A. Kudryavtsev, Comput. Phys. Commun. **180**, 339 (2009), (MUSIC), arXiv:0810.4635 [physics.comp-ph].

[90] L. Reichhart *et al.* (ZEPLIN-III), Astropart. Phys. **47**, 67 (2013), arXiv:1302.4275 [physics.ins-det].

[91] F. E. Gray, C. Ruybal, J. Totushek, D.-M. Mei, K. Thomas, and C. Zhang, Nucl. Instrum. Meth. **A638**, 63 (2011), arXiv:1007.1921 [nucl-ex].

[92] D.-M. Mei and A. Hime, Phys. Rev. **D73**, 053004 (2006), arXiv:astro-ph/0512125 [astro-ph].

[93] A. Lindote, H. M. Araujo, V. A. Kudryavtsev, and M. Robinson, Astropart. Phys. **31**, 366 (2009), arXiv:0810.1682 [hep-ex].

[94] D.-M. Mei, Z.-B. Yin, and S. R. Elliott, Astropart. Phys. **31**, 417 (2009), arXiv:0903.2273 [nucl-ex].